Distinct Quaternary States, Intermediates, and Autoinhibition During Loading of the DnaB-Replicative Helicase by the Phage λP Helicase Loader

†Abhipsa Shatarupa[1,2]†, Dhanjai Brown[1,2], Paul Dominic B. Olinares[5], Jillian Chase[1,2], Eta Isiorho[6], Brian T. Chait[5], and *David Jeruzalmi[1,2,3,4]

[1]Department of Chemistry and Biochemistry, City College of New York, New York, NY 10031, USA.

Ph.D. Programs in Biochemistry[2], Biology[3], and Chemistry[4], The Graduate Center of the City University of New York, New York, NY 10016, USA.

[5]Laboratory of Mass Spectrometry and Gaseous Ion Chemistry, The Rockefeller University, New York, New York 10065, USA

[6]Structural Biology Initiative, CUNY Advanced Science Research Center, New York, NY 10031, USA

*To whom correspondence should be addressed: 212-650-6062; dj@ccny.cuny.edu

†These authors contributed equally.

Graphical Abstract

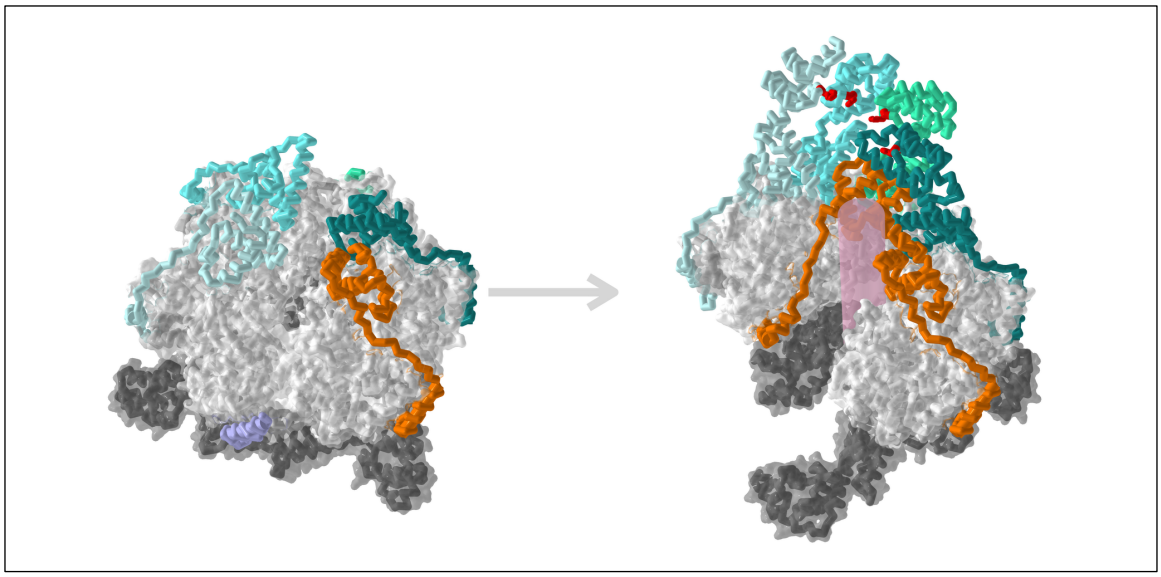

The DnaB helicase loading pathway at the phage λ replication origin populates two intermediate states, distinguished by the number of λP loaders present. The DnaB ring in the B_6P_6 complex is planar and partially open. Although it binds six copies of the λP loader, the ajar planar state of DnaB yields inchoate interactions with the loader. During the maturation of the complex, the planar state of DnaB is reconfigured into an open spiral in the B_6P_5 complex, which the pentameric λP ensemble now grips tightly. This transition required the eviction of one copy of the loader. Although the breach in the DnaB open spiral is sufficiently sized for entry of ssDNA into the internal chamber, the disposition of one λP chain loader across the single breached interface in DnaB effectively blocks the path to physiological replication origin-derived ssDNA. DnaB is depicted in white/gray ribbon format under a transparent surface. The λP chains are colored orange and shades of blue. The pink cylinder represents the expected path of ssDNA through DnaB.

Abstract

Replicative helicases require loader proteins for assembly at the origins of DNA replication. Multiple copies of the bacteriophage λP (P) loader bind to and load the *E. coli* DnaB (B) replicative helicase on replication-origin-derived single-stranded DNA. We find that the *E. coli* DnaB•λP complex exists in two forms: B_6P_5 and B_6P_6. In the 2.66 Å cryo-EM model of B_6P_5, five copies of the λP loader assemble into a crown-like shape that tightly grips DnaB. In this complex, closed planar DnaB is reconfigured into an open spiral with a sufficiently sized breach to permit ssDNA to enter an internal chamber. The transition to the open spiral involves λP-mediated changes to the Docking Helix (DH)–Linker Helix (LH) interface. The loader directly stabilizes the open spiral. Unexpectedly, one λP chain in B_6P_5 is bound across the breach, precluding entry of replication-origin-derived ssDNA into DnaB's central chamber. We suggest that the B_6P_6 complex is an early intermediate in the helicase activation pathway wherein neither the DnaB helicase nor the λP loader has attained its final form. DnaB in this complex adopts a partially open planar configuration, termed ajar planar. The partially ordered λP loader assembly features a much looser interaction with DnaB. The ssDNA and ATP sites in both complexes are in a configuration ill-suited for binding or hydrolysis. Our work specifies the conformational changes required for the intermediate B_6P_6 to transition to B_6P_5 on the pathway to recruitment by the initiator protein complex to the replication origin.

Introduction

Efficient separation of duplex DNA into single-strand templates for DNA synthesis is a crucial feature of chromosomal replication systems across all cellular domains of life (1–10). Separation is carried out by the replicative helicase, an oligomeric entity that encircles an internal chamber into which one strand of DNA is loaded while the second strand is excluded. ATP-dependent translocation along the included strand leads to the melting of the duplex. Since bacterial chromosomal DNA is an infinitely long polymer with no free ends, assembling replicative helicases on DNA requires specialized loader proteins.

In bacteria, the replicative helicase (DnaB in most bacteria (henceforth: DnaB), or DnaC in *B. subtilis*) assembles into a two-tiered, ring-shaped homohexameric ensemble around one of the two strands of dsDNA (11–13) (Figure 1 and Supplementary Figure 1 and reviewed in (9, 10, 14–17) and in Supplementary Information). Each DnaB protomer comprises two domains: an amino-terminal domain (NTD) and a carboxy-terminal domain (CTD), linked by a linker helix (LH) element. The NTD and CTD tiers adopt two configurations, termed dilated or constricted, distinguished by the diameter of the central chamber, among other features. Each CTD harbors a helical element, termed the docking helix (DH), which packs against the LH element of an adjacent CTD (11–13). ATP is bound at CTD interfaces, using Walker A and Walker B motifs furnished by one CTD and the arginine finger β-hairpin motif by an adjacent CTD to mediate hydrolysis. Residues from each CTD also contact the phosphate backbone of ssDNA within the inner chamber (18).

89 An extensive literature provides insights into the structure and function of
90 helicase loaders in bacteria, including *E. coli* DnaC, phage λP (Figure 1), *B. subtilis*
91 DnaI, phage T4 gene 59, phage SPP1 G39P, phage P2 B, DciA, and DopE (1, 7,
92 19–30). Several schemes for helicase assembly on nucleic acid substrates have
93 been described, referred to here as (1) ring-opening, (2) ring-forming, or (3) ring-
94 closing ((10, 31, 32) and Supplementary Information). Two well-studied bacterial
95 loaders, *E. coli* DnaC and phage λP, are ring-opening loaders; although unrelated
96 in sequence or structure, they implement similar loading mechanisms. Both
97 loaders share an overall architecture, featuring a globular domain attached to an
98 element termed the lasso or grappling hook (15, 33, 34). Both capture and remodel
99 closed planar DnaB into an open right-handed spiral, maintaining both tiers in the
100 constricted conformation. Both suppress DnaB's ATPase and DNA unwinding
101 activities (35–38). Remodeling creates breaches in DnaB's two tiers of sufficient
102 size to allow access to the inner chamber by physiological ssDNA substrates
103 produced by the remodeling of the replication origins by the replication initiator
104 protein (*E. coli:* DnaA or phage λ: O) (19, 39–41). The structural resemblance
105 between the two loaders is limited to an alpha helix in the lasso/grappling hook
106 element, positioned between the DH and LH helices of two adjacent DnaB
107 subunits. Remarkably, the protein chain direction of these elements diverges (λP:
108 N-C; DnaC: C-N); this unusual feature reflects convergent evolution (15).

109 Maturation of the replication origin complex into the replisome requires the
110 eviction of the DnaB-inhibiting loader. DnaC (34, 35, 42) and λP (43, 44) utilize
111 distinct biochemical mechanisms to evict the loader. In phage λ, the tight *E. coli*

112 DnaB-λP loader (BP) complex (37) necessitates the involvement of the host heat
113 shock factors DnaJ, DnaK, and GrpE (40, 45–48) to evict the loader and activate
114 the helicase.

115 The 4.1 Å single-particle cryogenic-electron microscopy (cryo-EM) structure
116 of the BP complex informed many aspects of the helicase loading reaction (15,
117 33). However, the limited resolution revealed ~50% of the structure of the λP
118 loader, as only the carboxy-terminal domains of the five protomers (B_6P_5) were
119 visible in the EM map (EMDB: 7076, PDB: 6BBM (33)). Furthermore, the amino
120 acid sequence of the λP loader could not be assigned to its structure, thereby
121 obscuring the helicase and loader interface. As such, the mechanisms of DnaB
122 remodeling, ATPase suppression, and ssDNA entry into the central chamber were
123 incompletely deciphered. We have determined three cryo-EM structures of the BP
124 complex to gain insights into these mechanisms. Two of these structures extend
125 the precision of the B_6P_5 complex to 2.66 Å and 2.84 Å; the 2.66 Å structure
126 provides a nearly complete model. In the B_6P_5 complex, one copy of λP is entirely
127 resolved, and the other four are nearly so. The resulting pentameric λP ensemble
128 is held together by an extensive interface between its previously invisible domain
129 II sub-structure. In B_6P_5, the DnaB NTD and CTD layers are in open spiral
130 configurations, with openings sufficient for ssDNA to access the central chamber.
131 However, unexpectedly, we find that one copy of λP (chain Z) binds across the
132 breach in the DnaB CTD tier to create a significant block to the entry of
133 physiological origin-derived ssDNA into the central chamber of DnaB.

A third structure (3.85 Å) revealed the first view of a BP complex with six copies of the λP loader (B_6P_6). The configurations of both DnaB and λP in the B_6P_6 entity are strikingly different. Both tiers of DnaB are essentially planar, with the NTD tier topologically closed and the CTD layer ajar relative to B_6P_5. The configuration of the six copies of the λP loader and DnaB in B_6P_6 implies an inchoate complex that has not reached its final form. We suggest that the ajar planar configuration in B_6P_6 is intermediate in the helicase loading pathway between the closed planar and open spiral forms of DnaB.

Materials and Methods

Constructs of the λP helicase loader

This work's biochemical and structural studies relied on a large set of λP constructs (Supplementary Table 1). DNA sequencing (Genewiz/Azenta) was used to verify the integrity of each construct. Extensive efforts identified soluble domains corresponding to the following constructions: amino acids 105:210, 105:205, 105:215, 105:220, 110:210, and 110:215. Each construct included an N-terminal (N-His) or C-terminal (C-His) hexahistidine tag for purification. The construct spanning residues 105:210 provided a sample suitable for X-ray crystallography.

Protein Biochemistry

Full-length *E. coli* DnaB•λP complex and DnaB were purified using the procedure described in (33), except that 0.2 mM ATP was used instead of 0.5 mM. In addition, full-length *E. coli* DnaB was further chromatographed over a 320 mL Superdex200 size exclusion column equilibrated in 20 mM HEPES-NaOH, pH 7.5, 450 mM NaCl, 5% glycerol (v/v), 2 mM DTT, 0.5 mM $MgCl_2$, 0.2 mM ATP. DnaB-

158 containing fractions were concentrated to 23.5 mg/mL, aliquoted, flash-frozen in
159 liquid nitrogen, and stored at -80°C until use.

160 The *E. coli* DnaB•λP-C-His complex was first purified over nickel-
161 nitrilotriacetic acid beads (Ni-NTA, Qiagen) equilibrated in 50 mM sodium
162 phosphate, pH 7.6, 500 mM NaCl, 10% glycerol (v/v), and 5 mM β-
163 mercaptoethanol (BME). After sequential washing with 25 mM, 50 mM, and 100
164 mM imidazole in the equilibration buffer, the partially purified DnaB•λP-C-His
165 complex was eluted using successive washes containing 250 mM and 500 mM
166 imidazole in the equilibration buffer. The complex was further purified using methyl
167 hydrophobic interaction chromatography as described in (33). Lastly, the complex
168 was concentrated to ~9 mg/mL, aliquoted, flash-frozen in liquid nitrogen, and
169 stored at -80°C until use.

170 A λP construct encompassing residues 105:210 was expressed in *E. coli*
171 BL21 (DE3) cells as described in (33), except the induction proceeded at 16°C for
172 16 hours. λP105:210 substituted with selenomethionine (SeMet) was prepared for
173 X-ray crystallographic studies as described in (49). Cells expressing N-His-
174 λP105:210 were lysed by sonication (60% amplitude; 3 min; 0.3 secs on, 0.6 secs
175 off, Fisher Scientific Model 500). λP105:210 was recovered in the lysis
176 supernatant, purified over Ni-NTA as described above, and over Superdex200
177 equilibrated in 100 mM NaCl, 10 mM Tris-HCl pH 7, 5% glycerol (v/v), and 5 mM
178 BME. Fractions containing N-His-λP105:210 were concentrated to 3.5 mg/mL,
179 aliquoted, flash frozen in liquid nitrogen, and stored at -80°C until use.

180 An N-His-tagged λO construct encompassing residues 156-299 was
181 expressed in *E. coli* BL21 (DE3) cells using ECPM1 medium (50) according to
182 standard techniques. After growth at 37°C to an OD600 of 0.6 – 0.7, IPTG was
183 added to 0.5 mM, and protein expression was allowed to proceed overnight at
184 25°C. Induced cells were resuspended in 20 mM Tris-HCl, pH 8, 500 mM NaCl,
185 and 5% (V/V) glycerol at a ratio of 5 mL per gram of cells and frozen at -80°C until
186 use.

187 Cells expressing λO-156-299-N-His were lysed by sonication (70%
188 amplitude; 3 min; 30 secs on, 30 secs off, Fisher Scientific Model 500). The
189 clarified supernatant was chromatographed over Ni-NTA beads equilibrated in 50
190 mM Tris (pH 7.5), 500 mM KCl, and 5% glycerol (v/v). Following two washes of
191 the Ni-NTA beads with equilibration buffer supplemented with 20 mM and 30 mM
192 imidazole, λO-156-299-N-His was eluted with 250 mM imidazole. Dialysis into 40
193 mM Tris pH 8, 50 mM NaCl, and 5 mM BME preceded chromatography over Fast
194 Flow Q (Cytiva). The Q column was developed with a gradient from 50 mM to 1
195 M NaCl in the above buffer. λO-156-299-N-His-containing fractions were
196 precipitated with 70% saturated ammonium sulfate, resuspended, and further
197 chromatographed over a 320 mL Superdex 200 size exclusion column,
198 equilibrated in 20 mM HEPES-KOH pH 7.5, 300 mM NaCl, 5% glycerol, and 5 mM
199 BME. λO-156-299-N-His containing fractions were concentrated to 2 mg/mL,
200 aliquoted, flash-frozen in liquid nitrogen, and stored at -80°C until use.

201 Protein biochemistry was performed at 4°C.

202 **X-ray structure determination of λP domain III (residues 105 – 210)**

203 N-His-λP105:210 in 100 mM NaCl, 10 mM Tris-HCl pH 7, 5% glycerol (v/v),
204 and 5 mM BME was thawed on ice and further concentrated to ~3.5 mg/mL (> 200
205 μM). High-throughput vapor diffusion (sitting drop) crystallization trials were
206 performed using an Art Robbins Gryphon liquid handling robot in the
207 Macromolecular Crystallization Facility (MCF) of the Structural Biology Initiative at
208 the Advanced Science Research Center, City University of New York. Crystals of
209 λP105:210 were prepared using the sitting drop vapor diffusion method by mixing
210 either 0.1, 0.2, or 0.4 μL of the protein solution and 0.2 μL of a series of
211 commercially available crystallization screens (Qiagen). Conditions that provided
212 initial hits were optimized using bespoke screens prepared at the MCF. Optimized
213 crystals for X-ray diffraction were grown at room temperature in a buffer containing
214 3 M–4 M NaCl with 0.1 M HEPES-NaOH, pH 7–8, and required 7 days to form.
215 SeMet-derivatized crystals were grown in the same manner. For X-ray diffraction,
216 crystals (>70 μm) were cryoprotected by adding 0.2 μL of LV CryoOil (MiTeGen)
217 directly to the crystallization drop before flash-freezing in liquid nitrogen.

218 Diffraction data for native and SeMet-derivatized N-His-λP105:210 crystals
219 were recorded at cryogenic temperatures at the 24-ID-E and 24-ID-C (respectively)
220 beamlines at the Northeastern Collaborative Access Team (NECAT) Center for
221 Advanced Macromolecular Crystallography at the Advanced Photon Source at
222 Argonne National Laboratory. Data from native crystals were measured using a
223 wavelength of 0.97918 Å to Bragg spacings of 1.86 Å. Data from SeMet-
224 derivatized crystals were measured at the Se K-edge (12,662 eV, λ = 0.97918 Å),
225 corresponding to Bragg spacings of 1.86 Å. Both native and derivatized

226 λP105:210 crystallized in space group $P3_121$, with the following cell parameters: a
227 = 49.731, b = 49.731, c = 70.772, alpha = 90°, beta = 90°, and gamma = 120°
228 (Supplementary Table 2). The Matthews coefficient (51) implied the presence of
229 one copy of λP105:210 in the crystallographic asymmetric unit.

230 Diffraction images were integrated and scaled with HKL2000 (52). Efforts
231 to determine the phases of the λP105:210 structure using molecular replacement
232 and various search models derived from the cryo-EM structure of the DnaB-λP
233 complex did not yield a reliable solution. However, the structure was determined
234 using the single anomalous dispersion (SAD) method on the SeMet-substituted
235 crystals, as implemented in the Autosol feature of the Phenix suite (53). AutoBuild,
236 phenix.refine, and visualization with Coot (54) facilitated the development of the
237 final model, which comprises residues 119 to 192 (residues 105 to 118 and 193 to
238 210 could not be visualized). The model exhibited a crystallographic R factor,
239 R_{work}/R_{free}, of 0.23/0.24.

240 **Native mass spectrometry (MS)**

241 The *E. coli* DnaB•λP•ssDNA•λO-156-299-N-His complex was assembled by
242 mixing 94.2 μL of 7.96 μM *E. coli* DnaB•λP complex in 20 mM Na-HEPES pH 7.5,
243 450 mM NaCl, 2 mM DTT, 0.5 mM $MgCl_2$, 0.2 mM ATP, 5% glycerol with 15 μL of
244 100 μM of an aqueous solution of a 43-nucleotide ssDNA (5'-
245 TGACGAATAATCTTTTCTTTTTTCTTTTGTAATAGTGTCTTTT-3') derived from
246 the DNA unwinding element (DUE) of Oriλ (38) for 20 minutes; the mixture was
247 prepared at a 1:2 molar ratio of BP:ssDNA. 53.1 μL of 212 μM λO in 20 mM
248 HEPES-KOH pH 7.5, 300 mM NaCl, 5% Glycerol, and 5 mM BME was added to
249 this mixture at a 15-fold molar excess relative to BP, and the mixture was incubated

250 for 20 minutes at 4°C. The volume of the reaction mixture was adjusted to 250 μL
251 by adding Milli-Q water and a buffer containing 2.5 M ammonium acetate (pH 7.5)
252 and 2.5 mM magnesium acetate. This yielded a sample containing 3 μM BP, 6 μM
253 ssDNA, and 45 μM λO in 500 mM ammonium acetate, 0.5 mM magnesium acetate,
254 ~170 mM NaCl, and ~2% glycerol. The complexes were incubated for an
255 additional 30 minutes at 4°C.

256 To purify the DnaB•λP•ssDNA•λO-156-299-N-His complex from
257 uncomplexed components, 200 μL of the above mixture was applied to 300 μL of
258 Ni-NTA beads equilibrated in 500 mM ammonium acetate pH 7.5, and 0.5 mM
259 magnesium acetate. After a 45-minute incubation at 4°C, the beads were
260 recovered by centrifugation and washed four times with 300 μL of 500 mM
261 ammonium acetate pH 7.5, 0.5 mM magnesium acetate, and 50 mM imidazole to
262 remove untagged species; each wash included a 30-second incubation at 4°C.
263 Bound complexes were eluted with three washes of 300 μL of 500 mM ammonium
264 acetate (pH 7.5), 0.5 mM magnesium acetate, 250 mM imidazole, and 0.01%
265 Tween-20. SDS-PAGE analysis confirmed the presence of the DnaB, λP, and λO
266 components. Complex-containing fractions were pooled, concentrated over a
267 100kDa molecular weight cut-off membrane (Spin-X UF Corning Concentrator,
268 500uL, 431481) at 15,000 RPM to 0.48 mg/ml, flash-frozen in liquid nitrogen, and
269 stored at -80°C.

270 A 200 μL volume of the DnaB•λP•ssDNA•λO-156-299-N-His complex was
271 thawed and concentrated using a Microcon centrifugal filter with a 100-kDa
272 molecular weight cut-off (MWCO) (Millipore). To remove residual imidazole, 150

273 μL of the native mass spectrometry (nMS)-compatible solution (500 mM
274 ammonium acetate, pH 7.5, 0.5 mM magnesium acetate, 0.01% Tween-20, pH
275 7.5) was then added to the concentrate for another round of centrifugation. To
276 ensure the complete removal of imidazole, the concentrated sample was then
277 buffer-exchanged into an nMS-compatible solution using a Zeba microspin
278 desalting column with a 40-kDa molecular weight cutoff (Thermo Scientific) before
279 nMS characterization.

280 For nMS analysis, an aliquot (2 – 3 μL) of the buffer-exchanged sample was
281 loaded into a gold-coated quartz capillary tip that was prepared in-house and was
282 electrosprayed into an Exactive Plus EMR instrument (Thermo Fisher Scientific)
283 using a modified static nanospray source (55). The nMS parameters used
284 included: spray voltage, 1.24 kV; capillary temperature, 150 °C; S-lens RF level,
285 200; resolving power, 8,750 at m/z of 200; AGC target, 1 x 10^6; number of
286 microscans, 5; maximum injection time, 200 ms; in-source dissociation (ISD10 V;
287 injection flatapole, 8 V; interflatapole, 4 V; bent flatapole, 4 V; high energy collision
288 dissociation (HCD), 200 V; ultrahigh vacuum pressure, 5.8 × 10^{-10} mbar; total
289 number of scans, 100. Mass calibration in positive EMR mode was performed
290 using cesium iodide. Raw nMS spectra were visualized using Thermo Xcalibur
291 Qual Browser (version 4.2.47). Data processing and spectra deconvolution were
292 performed using UniDec version 4.2.0 (56, 57). The following parameters were
293 used for data processing: Gaussian smoothing, 3; background subtraction,
294 subtract curve 10; smooth charge state distribution, enabled; peak shape function,

295 Gaussian; beta setting (degree of Softmax distribution): 50, Mass range: 50,000 –
296 500,000 Da.

297 The measured masses are B_6P_4: 419,942 Da, B_6P_5: 446,642 Da, B_6P_5 +
298 oriλ ssDNA: 460,056 Da, and B_6P_6: 473,318 Da. The observed deviations of the
299 measured mass from the expected mass ranged from 0.07% to 0.10% and were
300 due to peak broadening mainly from nonspecific magnesium adduction. In
301 addition, peaks corresponding to DnaB subcomplexes were found, including B
302 (52,269 Da), B_2 (104,551 Da), and B_3 (156,899 Da). Although nMS analysis
303 observed several BP assemblies, including a B_6P_6 complex and B_6P_5-ssDNA
304 species(33), cryo-EM analyses did not reveal the positions of ssDNA or the binding
305 of λO-CTD. PDBO performed all native MS analyses in the laboratory of BTC.

306 **ATPase rate measurements**

307 An NADH-coupled microplate spectrophotometric assay was employed to
308 measure the rates of ATP hydrolysis (58, 59) by *E. coli* DnaB and to investigate
309 the effect of λP on these rates. DnaB was maintained at a fixed concentration of
310 100 nM in all experiments. To assess the contribution of unrelated helicases that
311 may have co-purified with the various DnaB entities, we conducted control
312 experiments using a bacterial protein extract prepared according to the exact set
313 of steps described above for DnaB, except that the cells contained the pET24
314 vector, which did not include either the DnaB or λP genes.

315 NADH oxidation data were recorded in the presence of 2 mM ATP (GoldBio
316 A-081-100), 2mM phosphoenolpyruvic acid monopotassium salt (PEP), 0.01 U/μL
317 lactate dehydrogenase (Sigma-Aldrich, L1254), 0.002 U/μL pyruvate kinase
318 (Sigma-Aldrich, P7768],) and 0.3 mM NADH in the following buffer: 50 mM

319 HEPES-KOH, pH=7.5, 150 mM potassium acetate, and 8 mM magnesium acetate,
320 5 mM BME, and 0.25 mg/mL bovine serum albumin (BSA, Fisher #BP9706100).
321 The above components, except for ATP, were combined and placed into wells of
322 a Corning 96-well clear round-bottom UV-transparent Microplate (p/n: 3788). The
323 plate was then warmed to 37 °C for 5 minutes in a pre-warmed SpectraMax M5
324 plate reader (Molecular Devices). After the warming phase, endpoint readings
325 were taken at a 340 nm wavelength to enable measurement of the path length.
326 This was followed by the addition of 2 mM ATP, mixing through pipetting, and
327 immediately reinserting the plate into the plate reader. Absorbance data were
328 taken at 340 nm every 30 seconds over 30 minutes. Each experiment was
329 performed in triplicate. Raw data was imported into Microsoft Excel for analysis.
330 Each absorbance curve was manually inspected to identify the period during the
331 experiment wherein the slope of the 340 nm absorbance vs. time(s) was constant;
332 in all cases, this period was the complete 30-minute period. The slope of the
333 absorbance curve was obtained by calculating the difference between the final and
334 initial absorbance values and dividing by time in seconds. The resulting slope
335 value was divided by the extinction coefficient of NADH (6,220 M^{-1} cm^{-1}) and the
336 path length (cm) calculated by the plate reader. This calculation produced the rate
337 of ATP hydrolysis in M/s. After correcting for background by subtracting the blank,
338 this value was processed into ATPase activity in turnovers per second by
339 multiplying by the reaction volume ($2x10^{-4}$ L), dividing by the mass of DnaB (g) in
340 the assay, and then multiplying by the molecular weight of monomeric DnaB
341 (52,390 g/mol).

342 **Sample Preparation for Single Particle Cryogenic Electron Microscopy**

343 The BP complex in 20 mM HEPES-NaOH pH 7.5, 450 mM NaCl, 2 mM
344 DTT, 0.5 mM $MgCl_2$, 0.2 mM ATP, and 5% glycerol (v/v) and λO-156-299-NHis in
345 20 mM HEPES-KOH pH 7.5, 300 mM NaCl, 5% glycerol (v/v), and 5 mM BME
346 were diluted with glycerol versions of their respective holding buffers to a
347 concentration of ~0.25%.

348 Synthetic single-stranded DNA oligonucleotide 5'-
349 TGACGAATAATCTTTTCTTTTTTCTTTTGTAATAGTGTCTTTT-3' (38) (IDT) was
350 resuspended in Milli-Q water. BP-ssDNA complexes were prepared by mixing
351 protein (1.5 μM) and ssDNA (1.875 μM) at a 1.25 molar excess. BP•λO-156-299-
352 NHis•ssDNA complexes were prepared by mixing BP (1.5 μM) with ssDNA (1.875
353 μM) and λO-156-299-NHis (2.25 μM) at 1.25 and 1.5 molar excess, respectively.

354 Protein-DNA complexes were applied to ultra-gold foil grids with holey gold
355 support and 300 mesh size (R 0.6/1, Quantifoil Micro Tools GmbH); the grids were
356 flash-frozen as described (33) and stored in liquid nitrogen until use.

357 **Acquisition of Cryo-EM Data**

358 This work encompassed three single particle cryo-EM (cryo-EM) data sets:
359 1) the P45-J50 data set taken from samples that contained the BP complex bound
360 to ssDNA, 2) the P155-J148 data set recorded from the BP•λO-156-299-
361 NHis•ssDNA complex, and 3) the P11-J107 data set from BP complex bound to
362 ssDNA (sample identical to the P45-J50 dataset) (Supplementary Figures 2, 3, 4,
363 5, 6, 7, Supplementary Information and Supplementary Table 3). The P45-J50
364 data set produced a 2.66 Å map of the B_6P_5 complex. However, no ssDNA was
365 observed in the EM maps. The P155-J148 data set yielded a 3.85 Å model of the

366 B_6P_6 complex; however, our maps did not display the λO-156-299-NHis and
367 ssDNA components. The P11-J107 data set produced a 2.84 Å resolution map of
368 the B_6P_5 complex (Supplementary Information and Supplementary Methods).

369 All data were taken on the Titan Krios (FEI, Hillsboro, Oregon) operating at
370 an accelerating voltage of 300 kV and equipped with a Gatan K3 Summit (Gatan,
371 Pleasanton, California) direct electron detector. Data collection was managed by
372 Leginon (60–62). All movies were collected at a pixel size of 1.083 Å. 7,863
373 movies were measured for the P45-J50 BP-ssDNA complex with a defocus range
374 of -1 µm to -2.5 µm, 6,479 for the P155-J148 BP•λO-156-299-NHis•ssDNA
375 complex with a defocus range of -0.6 µm to -2.7 µm, and 25,595 un-tilted movies
376 and ~6661 tilted movies for the P11-J107 BP-ssDNA complex with a defocus range
377 of -1 µm to -2.5 µm and 1 µm to -4.5 µm, respectively. The 25°-tilted data set was
378 collected from the same grid to mitigate the expected preferred specimen
379 orientation (63); the tilted data set was measured using similar imaging parameters
380 to those of the un-tilted collection. The dose rate was set to 25.51 e-/Å²/s for P45-
381 J50, 25.59 e-/Å²/s for P155-J148, 25.51 e^-/Å^2/s for P11-J107 un-tilted collection,
382 and 25.78 e^-/Å^2/s for P11-J107 for 25°-tilted collection, resulting in accumulated
383 doses of 51.01 e-/Å², 51.19 e-/Å², 51.01 e^-/Å^2, and 51.55 e^-/Å^2, respectively. Forty
384 frames were recorded per movie at 0.05-second intervals over a total duration of
385 2 seconds. The 2.84 Å B_6P_5 model, derived from the P11-J107 data set, is
386 discussed in the Supplementary Information, as it is less complete than the 2.66 Å
387 model from the P45-J50 data set.

Unless otherwise indicated, cryo-EM data sets were processed in CryoSPARC (64–68). Processing was initiated for each dataset by applying patch motion correction and estimating the contrast transfer function (CTF).

Cryo-EM Image Processing of the P45-J50 Data Set (B_6P_5, 2.66 Å)

The 7,863 movie frames were submitted to particle selection using the 'Blob Picker' tool (Supplementary Figure 2). Inspection of the resulting 7,250,518 particles in the "inspect picks" job trimmed the data set to 3,762,436 particles. This set was extracted with a 300-pixel box size and 2x binning to produce 3,193,376 particles. 2D classification with a total of 200 classes yielded 2,448,342 particles. 2D templates prepared from this set were used in template picking to produce 10,556,526 particles. Another round of inspection in the "inspect picks" job reduced the number to 4,331,766 particles. Extraction with a larger box (400 pixels) and 2x binning produced 3,709,955 particles. These particles underwent a second round of 2D classification with 200 classes to produce 2,798,195 particles. *Ab initio* reconstruction with C1 symmetry enforced produced four classes, A-00, A-01, A-02, and A-03, with ~780K, ~473K, ~996K, and ~547K particles. Heterogeneous refinement of these classes resulted in four classes termed B-00, B-01, B-02, and B-03 (grey, red, pink, and blue in Supplementary Figure 2), with the following particle counts and map resolutions ~480K/4.40 Å, ~1.5 million/4.40 Å, ~283K/7.83 Å, and ~528K/4.40 Å. Class B-01, with the largest number of particles, was pushed forward to non-uniform refinement with the 'optimize per-particle defocus' parameter enabled to produce a 4.44 Å map. Particles from this map and the B-01 volume then went through a second round of non-uniform refinement with 'optimize per-group CTF params' enabled to produce a second

412 4.44 Å map. The particles from the second round of non-uniform refinement were
413 re-extracted with a larger and unbinned box size of 400 pixels to provide a new
414 collection of ~1.5 million particles. This revised set of particles and the class B-01
415 volume above were submitted to a third round of non-uniform refinement. This
416 calculation produced a 2.66 Å map (class D, green in Supplementary Figure 2).
417 Finally, class D underwent sharpening using DeepEMhancer (69).
418 DeepEMhancer generates maps by applying three algorithms: tight target, wide
419 target, and high-resolution. Inspection of these maps suggested that the wide
420 target was the best option regarding map quality (class E, magenta in
421 Supplementary Figure 2). Additional details about the final volume appear in
422 Supplementary Figure 3. Further processing of Class B-00 produced a 2.75 Å
423 map (class C). However, this map proved to be of lower quality than the 2.66 Å
424 map described above; as such, it was not further pursued.

425 **Cryo-EM Image Processing of the P155-J148 Data Set (B_6P_6, 3.85 Å)**

426 The 6,479 movie frames were submitted to particle extraction using Topaz
427 (70) and the pre-trained ResNet8 (64 units) model (Supplementary Figure 4). The
428 extracted particles were processed using the "inspect picks" job, resulting in
429 6,317,003 particles. They were then extracted with a 320-pixel box size and 2x
430 binning, yielding 5,694,258 particles. 2D classification with 200 classes produced
431 3,165,479 particles. *Ab initio* reconstruction with these particles, with enforcement
432 of C1 symmetry, resulted in five classes named I-00 to I-04, with 580K, 600K,
433 560K, 840K, and 585K particles in the various classes. Class I-03, with the highest
434 particle count, was submitted to Topaz training using the ResNet8 model

435 architecture. The trained Topaz model was then used to re-extract 2,315,940
436 particles using a 200-pixel box size (binned/Fourier cropped).

437 2D classification, and *ab-initio* reconstruction with C1 symmetry produced 4
438 classes: class II-00, II-01, II-02, and II-03 with ~422K, ~312K, ~315K, and ~472K
439 particles, respectively. Heterogeneous refinement of the above 4 classes
440 produced: class III-00, III-01, III-02, and III-03, with ~325K (4.40 Å), ~338K (4.40
441 Å), ~264K (4.40 Å), and ~590K (4.40 Å) particles/resolutions, respectively. Class
442 III-02 was not further processed because of its comparatively low particle count
443 and a distorted volume that appeared stretched in all directions and which could
444 not be reconciled with known structures of DnaB or the BP complex. Class III-03
445 volume appeared as a distinct two-tiered DnaB structure, whereas maps from
446 classes III-00 and III-01 resembled DnaB but lacked structural information.
447 Consequently, only the III-03 volume was selected for further refinement.

448 To refine the map further, 1,256,507 particles from all three classes (III-00,
449 01, and 03) were selected for the next round of heterogeneous refinement. Since
450 heterogeneous refinement requires multiple input maps of the same or different
451 types, we included the class III-03 volume three times. We chose the Class III-03
452 map because it was the most well-defined among all the Class III volumes and had
453 the highest number of particles. Heterogeneous refinement yielded three classes,
454 characterized by the following numbers of particles and resolutions: IV-00
455 (~354,000 particles, 4.40 Å), IV-01 (~581,000 particles, 4.40 Å), and IV-02
456 (~322,000 particles, 4.40 Å). These volumes are grey, pink, and green in
457 Supplementary Figure 4. Since multiple particle sets can be used, but only a single

volume can be provided for non-uniform refinement, particles from classes IV-00, IV-01, and IV-02 were combined, incorporating the class IV-01 volume with the highest particle count, and submitted to non-uniform refinement. The resulting volume (4.44 Å) was designated class V (blue in Supplementary Figure 4).

Refined particles from class V were used to extract 1,250,415 particles at a full box size of 400 pixels. Non-uniform refinement produced a 3.00 Å map (Class VI, red in Supplementary Figure 4). The 3.00 Å resolution, based on the Gold-Standard Fourier shell correlation (GSFSC) curve, was a positive outcome (not shown). However, the observation that the FSC curve did not drop to zero implied a potential problem, possibly due to the presence of duplicate particles. To address this potential problem, a "remove duplicates" job was applied, which retained ~573K particles while discarding ~678K particles. The retained particles were refined against the class V volume (blue), with the ‘optimize per-particle defocus’ parameter enabled to yield a 3.90 Å map. Non-uniform refinement and class V volume, with the ‘optimize per-group CTF params’ and the "fit tilt" and "fit trefoil" parameters, yielded a 3.91 Å map. A last round of non-uniform refinement using the refined particles from the 3.91 Å map and the class V volume, with the ‘optimize per-group CTF params’ and "fit spherical aberration" and "fit tetrafoil" provided a 3.85 Å resolution map (Class VII, purple in Supplementary Figure 4). The class VII volume was sharpened using DeepEMhancer (69). Inspection of the maps suggested that the tight target (class VIII, as shown in Supplementary Figure 4) had the best map quality. Additional details about the final volume appear in Supplementary Figure 5.

481 ## Model Building

482 **P45-J50 (B_6P_5, 2.66 Å).** To build a model of the B_6P_5 complex for refinement, we
483 leveraged the availability of high-resolution crystal structures of the amino-terminal
484 domain of DnaB• (PDB: 1B79, (71)), domain III of the λP (1.86 Å, this work), as
485 well as Alphafold models of both *E. coli* DnaB (72) and λP ((73, 74) and
486 Supplementary Information). We reasoned that a model constructed from high-
487 resolution components would provide an excellent starting stereochemistry and
488 perform best in a restrained real-space refinement against our 2.66 Å cryo-EM
489 map in Phenix (75, 76).

490 Components were placed with MOLREP (77, 78) or guided by an earlier
491 B_6P_5 structure (PDB: 6BBM, (33)). Notably, five λP domain II segments, missing
492 from earlier models, could be built into the P45-J50 map. Several segments of
493 DnaB and λP (DnaB residues: 25:30, 166:181, 500:501, and λP residues: 1:23,
494 78:82, 99:100, 120:122, 186:212, 226:232) could not be placed by superposition;
495 these were built by hand in COOT (79) using the Alphafold models as guides.
496 AlphaFold predicted a straight helix for the N-terminal lasso/domain I. However,
497 this conformation did not fit the density in our EM map, so the helix had to be bent
498 after Glu-14.

499 The final B_6P_5 model for the 2.66 Å P45-J50 map encompasses DnaB
500 residues (chain A: 25:173 and 201:468, chain B: 16:468, chain C: 19:468, chain
501 D: 18:468, chain E: 19:468, and chain F: 24:468) and λP residues (chain V: 40:232,
502 chain W: 40:232, chain X: 40:232, chain Y: 37:232, and chain Z-2:231). Our model
503 includes six ADP molecules bound to six magnesium ions. Although included in

the sample submitted to cryo-EM, the P45-J50 map showed no density that could be interpreted as ssDNA.

P155-J148 (B_6P_6, 3.85 Å). The P155-J148 map revealed a partially ordered B_6P_6 complex. A model of the complex was constructed using the approach described above for the P45-J50 map. The availability of the B_6P_5 model also guided model building. While the complete structure of each DnaB chain could be seen, only portions of the six λP loader chains were ordered. In four chains (V, W, Y, and Z), only domains III/IV were visualized; for two chains (U and X), only the C-terminal lasso/domain IV was seen. For all λP chains, the N-terminal lasso/domain I and domain II were disordered. The final model encompassed DnaB residues (chain A: 24:468, chain B: 24:468, chain C: 24:468, chain D: 24:468, chain E: 24:468, and chain F: 24:468) and six protomers of λP (U: 211:232, V: 119:232, W: 119:232, X: 210:233, Y: 119:232, Z: 119:231). Each nucleotide binding site in B_6P_6 is filled with ADP/Mg, though the occupancies are not identical. Although the C-terminal domain of λO (residues 156-299) and ssDNA were included in the sample submitted to cryo-EM, the P155-J148 maps showed no density for these entities.

Model Refinement

Models of the BP complexes described in this work were refined using the RealSpaceRefine tool in Phenix (75, 76) against either maps produced by CryoSPARC (64–68) and/or DeepEMhancer (69). Refinement encompassed cycles with minimization global, NQH flips, and the atomic displacement parameters (adp) options and leveraged Ramachandran and secondary structure restraints. The rigid body option was applied in the first round of refinement. The

527 rigid bodies for all DnaB chains in all the refinements were defined as follows:
528 residues 1:173 (NTD), 174:200 (LH), and 201:468 (CTD). For λP, the rigid bodies
529 were defined as follows: residues 1:40 (domain I), 41:118 (domain II), 119:192
530 (domain III), and 193:233 (domain IV), and applied only when the domain in
531 question was present in a particular model. The refinement of B_6P_6 performed
532 better when the 2.66 Å B_6P_5 (P45-J50) model was included as the reference
533 model. We also performed two rounds of model rebuilding with high-resolution
534 components, as described above, followed by re-refinement. This procedure
535 produced high-quality models with excellent statistics, particularly in the less well-
536 defined segments.

537 **Model Analysis and Visualization**

538 Structural analysis was carried out using the CCP4 software package (80),
539 Coot (79, 81), the Uppsala software suite (82–85), UCSF-CHIMERA (86), Phenix
540 (53, 75, 76, 87–91), PyMOL (92), and as described previously (33). Distances and
541 angles within and between protein structures were calculated using the PyMol
542 Python scripts titled "pairwise_dist"
543 (https://pymolwiki.org/index.php/Pairwise_distances) and
544 "angle_between_domains"
545 (https://pymolwiki.org/index.php/Angle_between_domains). Molecular graphics
546 and figures were generated using UCSF-CHIMERA (86) and PYMOL (92). The
547 software used in this study was sourced from the SBGrid Consortium (93).

548

549 # Results

550 ## Two States (B_6P_5, B_6P_6) of the *E. coli* DnaB Helicase–λP Loader Complex

551 This work aimed to obtain cryo-EM (94–97) structures of the *E. coli* DnaB–
552 λP Helicase Loader (BP) complex bound to ssDNA and, separately, bound to
553 ssDNA and the carboxy-terminal domain of the λO initiator protein (λO-CTD). We
554 have determined three cryo-EM structures at 2.66 Å, 2.84 Å, and 3.85 Å (Methods,
555 Supplementary Figures 2, 3, 4, 5, 6, 7, Supplementary Information, Supplementary
556 Methods, and Supplementary Table 3). These analyses yielded EM maps of
557 higher resolution than our previous 4.1 Å study of the B_6P_5 entity (33) and provided
558 a first look at a second oligomeric form of the BP complex (B_6P_6). Native mass
559 spectrometry (nMS) analysis of these samples showed the presence of a B_6P_5
560 ssDNA assembly (33) and a B_6P_6 species (Supplementary Figure 8). However,
561 cryo-EM analyses did not reveal the positions of ssDNA in any of the complexes.

562 Our earlier study provided limited insights into the λP loader, as only the
563 carboxy-terminal domains (domains III and IV) were visible in our maps. We were
564 further limited by a model that lacked protein side chains, since the amino acid
565 sequence could not be assigned to the map. The 2.66 Å cryo-EM map of the B_6P_5
566 complex revealed a nearly complete structure of five copies of the λP loader
567 (Figure 2 and Supplementary Figure 9). One λP chain was entirely seen (chain Z;
568 residues 1:233, Supplementary Figure 10), and four chains were nearly completely
569 visible (Domains II, III, IV, chains V, W, X, and Y; residues ~40:233). Our maps
570 did not resolve four instances of λP domain I (chain V, W, Y, and X; residues
571 1:~39). In the nearly complete model, the B_6P_5 complex presents as a four-tier
572 entity with its λP and DnaB components arranged in a right-handed open spiral

573 configuration (Figure 3) whose architecture differs from the translocating form of
574 DnaB (18). A prominent breach is visible between the top and bottom of the open
575 DnaB spiral (Figure 2 and Supplementary Figure 11). The two additional tiers
576 constitute domains I/II and III/IV of λP; the remaining two are the NTD and CTD of
577 DnaB (Figure 2). The NTD and CTD tiers of DnaB in the B_6P_5 complex are in the
578 constricted configuration (Supplementary Figure 1 and Supplementary
579 Information). In the B_6P_5 complex, the six nucleotide sites on DnaB are filled with
580 ADP, although the site on chain B at the top of the spiral appears to have lower
581 occupancy (Supplementary Figure 12). As noted previously (15, 33), the open
582 spiral geometry of DnaB within the B_6P_5 complex leaves the ATP hydrolytic
583 catalytic machinery in positions sub-optimal for catalysis (Supplementary
584 Information and Supplementary Figure 13). The 2.84 Å B_6P_5 structure
585 superimposes with the 2.66 Å instance with an RMSD of 0.7 (3043 Cα) and is more
586 fully described in the Supplementary Information.

587 Previously, we used nMS to demonstrate that preparations of the *E. coli*
588 DnaB–λP helicase loader contained a second oligomeric form with a B_6P_6
589 stoichiometry ((33) and Supplementary Figure 8); our 3.85 Å cryo-EM map
590 revealed the atomic structure of this complex. Models corresponding to domain
591 III/IV were built for four of the six λP chains (V, W, Y, and Z); for the remaining
592 chains (U and X), only the domain IV-C-terminal lasso was visible in our maps. In
593 contrast to the open spiral seen in the B_6P_5 complex, DnaB in the B_6P_6 complex is
594 nearly planar, with no breach. Below, we provide evidence that DnaB in this
595 complex is partially open, with four of its CTDs further away from their neighbors

596 than in closed, planar DnaB. Unlike B_6P_5, the NTD DnaB in the B_6P_6 complex is
597 in the dilated configuration, while the CTD tier is constricted. The six nucleotide-
598 binding sites in B_6P_6 are filled with ADP, although judging from the density quality,
599 the occupancy of each site differs (Supplementary Figure 12).

600 **The Pentameric λP Ensemble in B_6P_5 Keeps DnaB's Inner Chamber Sealed**

601 In the nearly complete 2.66 Å B_6P_5 complex, five copies of λP assemble in
602 a crown-like shape on top of the CTD layer to effectively seal the breach in the
603 DnaB spiral, thereby preventing entry by physiological replication origin ssDNA
604 (Figure 2). Each monomer of λP features four domains: two compact domains
605 (domain II: residues ~30 to ~119; domain III: residues ~120 to ~192) flexibly linked
606 (Supplementary Figure 10). The amino (domain I, residues 1 to ~29) and carboxy
607 termini (domain IV, 193 to 233) of λP are likely intrinsically disordered in solution
608 but fold into an alpha helix linked to domains II and III by an extended segment;
609 we refer to these elements as the N-terminal and C-terminal lasso/grappling hooks.
610 The five previously unseen copies of the λP domain II assemble into an open spiral,
611 displaying an extensive interface that stabilizes the pentameric λP ensemble on
612 the B_6P_5 complex. The λP domain II average of ~1000 $Å^2$ of surface area for a
613 total of ~4000 $Å^2$ for the complete ensemble. These values are significant when
614 considered in the context of the NTD (average: ~1900 A^2) and CTD (average:
615 ~2300 A^2) interfaces of DnaB. The five λP domain IIs circumscribe a volume
616 continuous with DnaB's inner chamber and exhibit modest flexibility relative to the
617 corresponding domain III position (Supplementary Figure 14). Five domains III/IV
618 of the λP loader ensemble bind at DnaB subunit interfaces; notably, five C-terminal
619 lasso/grappling hooks bind at the nexus of DnaB's DH and LH elements. As

predicted (15, 33), there are no contacts between the B_6P_5 complex's five copies of λP domain III. Superposition suggests that domains III/IV are relatively rigid due to their contact with DnaB (Figure 5, Supplementary Figure 14, and below).

One λP chain (Z) is entirely visible in our maps and, remarkably, adopts a configuration that the other chains cannot access. λP chain Z is positioned to span and effectively block the breach in the open DnaB spiral through its contacts to the A, B, and F subunits. The N-terminal lasso (domain I) of λP binds to chain B at the top of the open DnaB spiral (in the pose in Figure 2). A single breach in DnaB implies that only domain I of one chain can adopt the configuration of the λP chain Z; the remaining domain Is, disordered in our structure, must populate distinct configurations. Notably, Tyr 27 in λP domain I makes a close contact with the ADP in the chain B CTD; the role, if any, of nucleotide in stabilizing the B_6P_5 complex requires clarification. Domain II spans the breach between subunits B and A at the top and bottom of the spiral, respectively. Finally, Domain III/IV binds at the interface between the CTDs of subunits A and F. Crucially, the position of the breach-blocking domain II of λP chain Z is maintained through the extensive interface between the five domain IIs of the ensemble (chains V, W, X, Y, and Z). Thus, even though openings in the NTD and CTD tiers of DnaB provide entrances for ssDNA of sufficient size (NTD: ~7.8 Å; CTD: ~10.5 Å; Figure 2 and Supplementary Figure 11), the disposition of chain Z, along with the extensive interface between the five domain IIs, effectively seals entry into DnaB's inner chamber to a physiological ssDNA bubble-shaped substrate at a replication origin (Figure 1).

643 Comparisons of the higher resolution B_6P_5 model with the *E. coli*
644 DnaB•DnaC (B_6C_6) complex (15, 33, 34) show that the single-ordered N-terminal
645 lasso/grappling hook (domain I) of λP-chain Z positions the N-terminal helix of this
646 element against the DH helix of DnaB chain B; this position overlaps with the
647 lasso/grappling hook of DnaC, which is bound at the same site (Figure 4 and
648 Supplementary Figure 15). Notably, although the binding modes of λP's five C-
649 terminal lassos are identical and resemble those of DnaC, save for the change in
650 protein chain direction, the N-terminal lasso binds to the DH helix via a binding
651 mode that differs from that seen with the C-terminal lasso (Supplementary Figure
652 16). Interestingly, one λP protomer (chain Z) binds at the top and bottom of the
653 breach (in the pose in Figure 2), using the N-terminal and C-terminal lassos,
654 respectively. However, in the DnaC complex, these functions are carried out by
655 two distinct protomers, chain G and chain L, at the top and bottom of the spiral.
656 For both loaders, positioning cognate elements on the DnaB chain B at the top of
657 the spiral could sterically suppress the re-closure of the helicase. This finding
658 represents another example (15) wherein the unrelated λP and DnaC helicase
659 loaders have evolved to converge on the same solution: positioning a loader helix
660 in a similar but distinct binding mode on the DH element at the top of the DnaB
661 spiral.

662 Our 2.66 Å model of the B_6P_5 complex forces reconsideration of the
663 mechanism of helicase loading. The finding that one λP protomer binds across
664 the DnaB breach and blocks access of ssDNA to the inner chamber implies a
665 previously unrecognized autoinhibited configuration. Our results predict that

666 remodeling of the B_6P_5 complex to clear the path for ssDNA into the DnaB hexamer
667 must accompany the recruitment of the B_6P_5 complex to the replication origin.

668 **The Pentameric λP Loader Ensemble Grips DnaB Tightly**

669 In the B_6P_5 complex, the pentameric λP loader ensemble grips the DnaB
670 helicase at five discrete and widely dispersed sites (Figure 5); each site comprises
671 a DnaB-specific insertion into the RecA-fold (Supplementary Figure 17). Owing to
672 the asymmetry of the complex, not every λP instance uses every site. The five
673 sites on DnaB are 1) the DH element (residues 291:307) on chain B of the
674 breached interface (its partner LH element from chain A is not visible in our maps);
675 the N-terminal lasso of chain Z is the only λP element to make this contact (BSA:
676 ~1900 $Å^2$). This contact explains the finding that deletion of λP residues 9:85
677 disrupts the complex (98). 2) A short DnaB helix comprised of residues 387:391
678 on the CTD at the breached interface; this contact is only made by domain II of λP
679 chain Z (BSA: ~400 $Å^2$). 3) A wide patch that spans two adjacent DnaB CTDs
680 (residues 424:434, 456 on one CTD and residues 391:395, 429:430, 446:449, and
681 the C-terminal residue 468 from the adjacent CTD) and includes contacts (residues
682 447:450) on the arginine finger β-hairpin of each CTD; domain III of each λP
683 monomer contacts this patch (BSA: ~1600 $Å^2$). The involvement of the extreme
684 C-terminus of DnaB in λP contacts was anticipated by genetic experiments (99).
685 4) a site comprised of the DH (residues 290:307) and LH (residues 182:199)
686 elements of two adjacent DnaB subunits; the C-terminal lasso of each λP monomer
687 makes this contact (BSA: ~1400 $Å^2$). Notably, the nature of the DnaB•λP interfaces
688 at sites 1 (λP N-terminal lasso) and 4 (λP C-terminal lasso), both of which include
689 DnaB DH elements, diverge considerably; indeed, the N-terminal lasso occupies

690 the same space as that of the chain B LH element (Figure 4 and Supplementary
691 Figure 16). 5) A patch on the NTD of DnaB (residues 76:77, 183:195); two λP's
692 (chain Y and chain W) make this contact (BSA: ~350 $Å^2$). Our structure provides
693 a partial rationale for the finding that specific DnaB mutants (residues V256I/E426K
694 and G338E/E426K (98)) exhibit resistance to inhibition by λP, as residue 426 is
695 located at interfacial site #3. Residues 256 and 338 are packed against one
696 another in the CTD but are distant from the B_6P_5 interface; we speculate that
697 mutations at these sites disrupt the CTD's structure. The λP domain IIs of four
698 chains (V, W, X, and Y) make no contact with DnaB.

699 The extensive interface between the λP ensemble and DnaB contrasts with
700 the considerably more modest interface formed by the DnaC loader assembly (15,
701 33, 34). The six N-terminal lassos/grappling hooks of DnaC make identical
702 interactions with the DH-LH interface of each DnaB subunit: this binding site
703 overlaps with site #4 of the BP complex. Unlike domain III of λP, which slightly
704 overlaps with the position of the AAA ATPase domains of DnaC, the latter domain
705 makes no contact with DnaB. In this context, it is noteworthy that λP's higher
706 affinity to DnaB, which can displace DnaC from the BC complex (37), may be
707 explained by the multitude of contacts to DnaB made by the λP ensemble,
708 especially chain Z.

709 **The λP Ensemble Stabilizes the DnaB Spiral in the B_6P_5 Complex**

710 An extensive interface between helicase and loader stabilizes the right-
711 handed open DnaB spiral in the B_6P_5 complex (Figures 2, 3, 5, 6, and
712 Supplementary Figure 15). Domain III of each λP loader contacts two consecutive
713 DnaB subunits (interaction sites #2 and # 3). λP residues: 145:162 contact DnaB

714 loops (residues: 424:432) on one subunit, while λP residues: 131:141 and 169:174
715 of the same chain contact a DnaB loop (residues: 391:398) and a strand (residues:
716 447:449, 454:456, and 468) on a neighboring subunit.

717 Although the DnaC and λP loaders are unrelated in structure, the DnaB
718 portion of the B_6C_6 (34) and B_6P_5 (33) complexes adopts very similar right-handed
719 open spiral configurations (15). However, the underlying arrangement of the CTDs
720 is not identical; this divergence is reflected in the distinct helical parameters of each
721 CTD spiral (Figure 3, B_6P_5: average helical pitch (12.6 Å), rise (3.7 Å), and twist
722 (56.4°); B_6C_6: average helical pitch (15.8 Å), rise (4.2 Å), and twist (55.4°). This
723 distinct architecture arises from wedging apart the two CTDs in each B_2P_1 sub-
724 structure by ~3° relative to the arrangement seen in the BC complex; this translates
725 into small shifts in CTD positions (Figure 6). The disposition of DnaB subunits in
726 the B_6P_5 complex directly results from the unique interface made with λP. The
727 pentameric λP ensemble features an extensive interface with the helicase, and the
728 contacts mediated by λP domain III mediate the wedging apart of DnaB subunits.
729 On the other hand, the globular domains of the hexameric AAA+ DnaC ensemble
730 make no contacts with DnaB whatsoever; the absence of contacts permits a closer
731 approach of individual DnaB subunits to each other in the BC complex than is
732 possible in the B_6P_5 ensemble.

733 The observation of similar helicase configurations in the B_6P_5 and B_6C_6
734 complexes led us to previously suggest that the open spiral might be an intrinsic
735 DnaB state since it is observed in complexes with a loader that forms an extensive
736 interface (λP) and one that does not (DnaC) (15, 33, 34). The 2.66 Å B_6P_5 complex

structure teaches that the open spiral configuration may be intrinsic; however, the interaction with λP also drives changes in the spiral that are not seen when DnaC binds to DnaB. Whatever the source, an overall consequence of the inability of DnaB subunits in the B_6P_5 or B_6C_6 complexes to approach each other optimally has profound implications for both ATP hydrolysis and ssDNA binding (Supplementary Information and Supplementary Figures 13 and 18).

The Carboxy-Terminal Lasso of the λP Ensemble Shears the LH-DH Interface of Each DnaB Monomer in the B_6P_5 Complex

During the transition from the closed planar to the open spiral form (B_6P_5), each C-terminal lasso helix of the λP ensemble binds alongside 5 DH - LH elements to create a three-helical bundle (interaction sites #4 and #5), binding shears and nearly completely disrupts the underlying DH-LH interface (Figures 5 and 7). Notably, the DH and LH elements are unique to the DnaB family of helicases compared to other RecA family members ((100), Supplementary Figure 17). As noted above, the N-terminal lasso of λP binds to the sixth DH element (chain B) in DnaB (top of the spiral as in the pose in Figure 2); this DH element lines the breach in the hexamer (interaction site #1). Binding wholly expels the partner LH element (chain A) since the N-terminal lasso-helix takes its place; indeed, the sixth chain A LH helix is not seen in our EM maps.

In the closed planar form, the DH element of each DnaB subunit packs against the LH element of an adjacent monomer in an antiparallel fashion via an interface whose Cα atoms are, on average, ~15.2 Å apart (the closed planar forms have the following values: 4NMN (constricted): 14.7 Å, 2R6D (dilated): 15.4 Å, 3BGW (constricted): 15.5 Å). In closed planar *E. coli* DnaB (modeled on the 4NMN

761 structure (12)), the underlying contacts between the DH and LH elements are
762 mediated primarily by hydrophobic interactions (Figure 7). For example, DH
763 residue Trp 294 packs into a pocket formed by LH residues Val 190, Ile 193, and
764 Phe 197 on an adjacent DnaB subunit. DH residue Met 301 packs in a pocket
765 comprised of LH residues Leu 186 and Val 190, and DH residue Leu 305 binds in
766 a pocket lined by Ala 183 and Leu 186.

767 Our prior work showed that the DH-LH interfaces in both the B_6C_6 (34) and
768 the B_6P_5 complexes (15) are disrupted by the DnaC and λP loaders. In the 2.66 Å
769 B_6P_5 structure, we observe that the helical segment (residues 211:227) of each C-
770 terminal lasso of λP is positioned alongside the DH-LH elements. Compared to
771 the closed planar form, the DH and LH helices are rotated by an average of +8.0°
772 and ~-3.7 °, respectively, and translated by ~2.4 Å from ~14.7 Å in the closed
773 planar form to ~17.1 Å in the λP-induced open spiral (Figure 7). A critical overall
774 consequence of λP binding is the near-complete abrogation of interactions
775 between the DH and LH elements in the DnaB open spiral. The repositioned DH
776 and LH elements combine with the λP C-terminal lasso helix to produce a three-
777 helix assembly; the disrupted DH-LH interface is replaced with distinct contacts
778 between each component and residues in the λP C-terminal lasso helix. In the
779 repositioned DH element, DnaB Trp 294 packs against λP residues Ala 215, Lys
780 218, and Ile 219; DH residue Met 301 resides next to λP residues Ile 222 and Phe
781 226; DH residue Leu 305 contacts λP residue Phe 226 as it maintains contacts
782 with LH residue Ala183 (the sole contact between DH and LH in the loader
783 complex). The repositioned DnaB LH elements also contact the λP C-terminal

784 lasso helix. LH residue Glu 194 contacts Ile 219. Notably, the DH-LH-λP three-
785 helix bundle interaction is nearly identical in all five instances of B_2P_1 in the B_6P_5
786 complex (DnaB CTD: RMSD = 0.2 Å on 200 Cα atoms, Supplementary Figure 14).
787 We found that, although not included in the superposition, the second CTD DnaB
788 in the B_2P_1 sub-structure and domain III/IV of the λP superimpose well; this
789 suggests a relatively rigid DnaB-CTD_2-λP substructure in B_6P_5 (Supplementary
790 Figure 14).

791 Unlike the four λP protomers (chains V, W, X, and Y), which contact two
792 DnaB subunits, chain Z contacts three DnaB chains (B, A, and F). The interaction
793 with chain B at the top of the spiral (as in the pose in Figure 2) is mediated by the
794 N-terminal lasso helix of λP, which is positioned adjacent to the DH element that
795 lines the breach in the hexamer. In contrast to the three-helical DH-LH-λP bundle
796 seen with the five instances of the B_2P_1 sub-structure, a two-helical bundle is
797 observed (Figure 2 and Supplementary Figure 16). In this species, the LH element
798 (chain A) has been displaced and is not visible in our maps; in its place, we find
799 the λP N-terminal lasso helix. Notably, the same DnaB (chain B) DH residues
800 highlighted above (Trp 294, Ile 297, Met 301, and Leu 305) participate in the
801 divergent interaction with the N-terminal lasso helix of λP. DnaB DH residue Trp
802 294 contacts λP residue Met 16; DnaB residue Ile 297 packs against Gln 15; DnaB
803 residue Met 301 packs into a pocket formed from λP residues Met 8, Phe 11, Asp
804 12. Finally, DnaB residue Leu 305 is found in a pocket formed by Met 8 and Val
805 9. The resolution of our maps is relatively low in the volume encompassed by site

806 #1; as such, a description of the underlying interface should be considered
807 tentative.

808 Examining the configuration of various DnaB structures suggests that the
809 DH-LH interface is an essential nexus of structural changes during helicase
810 loading. Measurements of the distances between DH and LH elements in the
811 closed planar forms of Stage I (dilated: 2R6D (13) and constricted: 3BGW (11) and
812 4NMN (12)) reveal a ~15.2 Å separation. In the Stage II DnaC loader bound
813 conformers, with and without ssDNA, the distance between DH and LH elements
814 increases to ~17.4 Å and 17.8 Å; these values closely follow the ~17.1 Å distance
815 seen in the 2.66 Å B_6P_5 complex structure. With the expulsion of the loader and
816 transition to the translocating Stage IV, the DH and LH elements move closer
817 together (4ESV (18): 15.5 Å, 7T20:16.0 Å (101), 7T21:16.1 Å (102), 7T22: 16.1 Å
818 (103), and 7T23: 16.2 Å (104)), but perhaps, not as close as the Stage I structures.
819 Notably, in *V. cholerae* (VC), isolated (PDB: 6T66, (105)) and DciA-bound DnaB
820 (PDB: 8A3V, (26)) diverge from the above trends. The average DH–LH distance
821 in isolated closed planar VC DnaB is ~17 Å, close to values extracted from loader-
822 bound open spiral forms of DnaB. Furthermore, this distance appears to contract
823 (15.6 Å) in the DciA-bound closed planar form of DnaB. Divergences in distances
824 between DH–LH elements may suggest substantially different loader mechanisms
825 between the DnaC/λP and the DciA helicase loading systems. Notably, the
826 moderate resolution (2.8–3.8 Å) of the available structures limits our analysis.

827 Our work establishes the helical DH—LH DnaB elements as important
828 moving parts in the loading pathway. The binding of the λP loader disrupts the

829 hydrophobic packing seen in the DH—LH element of the closed planar
830 configuration, yielding two new interfaces between the same surfaces of each
831 component and the C-terminal lasso. A distinct interaction is seen between the
832 DH elements and the λP N-terminal lasso.

833 **Where Does the B_6P_5 Complex Bind ssDNA?**

834 DnaB and the λP loader are known to interact with ssDNA (18, 38, 106);
835 however, the mechanism by which these contacts are integrated within the
836 helicase loader complex remains unknown. We had previously shown that the
837 ssDNA binding site on DnaB is disrupted compared to the translocating complex
838 (15, 33) (Supplementary Information and Supplementary Figure 18). The 2.66 Å
839 structure of the B_6P_5 complex teaches that not only is the ssDNA binding site
840 disrupted in the loader complex, but two other architectural features sever access
841 to the central chamber. First, as described above, one λP monomer (chain Z)
842 binds to two DnaB subunits that span the breach, and in doing so, utilizes λP
843 domains I/II to physically block the entry of ssDNA into the chamber. Second,
844 owing to contacts between λP domain III and DnaB, the central chamber cannot
845 achieve the active form while the loader remains bound (Supplementary Figure
846 19). As noted above, for DnaB in the B_6P_5 complex to achieve the configuration
847 in the ssDNA complex, each CTD must rotate by ~15° toward the central chamber.
848 However, this structural change is precluded due to the steric clash between each
849 λP domain III and pairs of DnaB CTDs in the ssDNA complex. This finding starkly
850 contrasts with the B_6C_6 complex, where DnaC's divergent binding mode places no
851 restriction on the adoption by DnaB of the conformation in the ssDNA complex.
852 Indeed, in the B_6C_6-ssDNA complex (PDB: 6QEM, (34)), DnaB adopts a

853 configuration closely related to that in the ssDNA-bound translocating form (PDB:
854 4ESV, (18)). Notwithstanding its internal chamber's distorted shape and geometry,
855 the B_6P_5 complex is known to bind ssDNA robustly (Supplementary Figure 8 and
856 (33, 38)).

857 Little is known about the binding modes that λP deploys to bind ssDNA.
858 Although λP contains no known ssDNA binding domains, one λP residue (F99)
859 has been shown to crosslink to ssDNA (38, 106). In the B_6P_5 complex, the five
860 instances of λP F99 trace a winding path in the inner chamber formed by the λP
861 domain IIs (Figure 8). This finding implies that, notwithstanding the restrictions to
862 entry and binding of ssDNA in DnaB's central chamber, the λP loader contacts
863 nucleic acid in its inner chamber at some point during the helicase loading
864 pathway. Since linear ssDNA was used for crosslinking, little light is shed on the
865 process of loading onto the initiator-produced bubble at a replication origin.

866 Our structural findings raise several intriguing possibilities: 1) the λP loader,
867 while bound to DnaB, contributes most, if not all, of the significant contacts to
868 ssDNA, and 2) ssDNA is bound by DnaB but not in the central chamber. Such a
869 distinct ssDNA binding mode is hinted at by the blocked entry path into the central
870 chamber of the B_6P_5 complex and its distorted central chamber shape. Of course,
871 the B_6P_5-ssDNA complex may blend both modes. Supporting the notion that
872 DnaB interacts with surfaces outside the central chamber during the initial ssDNA
873 encounter complex, prior work by Trakselis and colleagues provides ample
874 evidence for the existence of such contacts (107, 108). Clarifying the path of

875 ssDNA through the B_6P_5 complex and whether it changes during the loading
876 reaction is an urgent priority for future studies.

877 Six Copies of λP Program a DnaB Intermediate between Closed Planar and 878 Open Spiral

879 In the B_6P_6 assembly, the DnaB and the λP loader components adopt
880 significantly different arrangements than in B_6P_5 (Figure 9). DnaB exhibits two
881 main configurational changes relative to its counterpart in B_6P_5. First, in contrast
882 to the open spiral in B_6P_5, the CTD tier in B_6P_6 is essentially planar (B_6P_6: average
883 helical pitch (~2.0 Å), rise (~0.5 Å), and twist (~60°) (Figure 3). Moreover, although
884 individual CTDs are ~2 Å further apart in B_6P_6 (average = 35.2 +/- 0.8 Å) than in
885 B_6P_5 (average = 33.1 +/- 0.1 Å), the CTD layer features no breach (Figure 9). We
886 refer to this configuration as the 'ajar planar' configuration. The higher standard
887 deviation in the distance measurement implies that DnaB in B_6P_6 is transitioning
888 between the relatively rigid closed planar and open spiral forms (Supplementary
889 Figure 20). Second, the NTD tier in B_6P_6 is found in the closed planar dilated
890 configuration (Figure 9), in contrast to the constricted arrangement in B_6P_5. The
891 NTD tier from B_6P_6 resembles those from 2R5U (109) (root mean square deviation
892 (RMSD) = ~2.0 Å) and 7T20 (101) (RMSD = ~1.0 Å).

893 The ajar planar form of DnaB in B_6P_6, like B_6P_5, exhibits distortions in the
894 interfacial nucleotide binding sites and the ssDNA binding site in the internal
895 central chamber (Supplementary Figures 13 and 18). The six nucleotide binding
896 sites in B_6P_6 are filled with ADP/Mg^{2+}, although the occupancy of the sites on
897 chains B, C, and D is lower than that of the other chains (Supplementary Figure
898 12). As noted above, pairs of DnaB subunits are further apart, a finding upheld by

899 the average distance between the Walker A lysine from one subunit and the
900 arginine finger β-hairpin from the adjacent subunit (B_6P_6: ~15 Å; B_6P_5: ~12 Å;
901 4ESV: 11.4 Å). Therefore, the interfacial NTP sites on B_6P_6, like those on B_6P_5,
902 are not positioned appropriately for hydrolysis (Supplementary Figure 13). Indeed,
903 our preparations of the BP complex, a mixture of B_6P_4, B_6P_5, and B_6P_6 (33),
904 displayed no detectable traces of ATP hydrolytic activities (Supplementary Figure
905 21).

906 Compared to their positions in the closed planar, open spiral, and closed
907 spiral ssDNA complexes, the seven DnaB residues in contact with ssDNA are
908 significantly displaced in B_6P_6 (Supplementary Figure 18). The distances between
909 one of these positions (*E. coli* Arg 403) in B_6P_6 and the corresponding residue (*B.st*
910 4ESV: Arg 381) in the translocating form are shifted between 6.3 Å and 39.1 Å
911 (Supplementary Figure 18B). Like the B_6P_5 ensemble, the ssDNA binding surface
912 in B_6P_6 diverges substantially from its configuration in the ssDNA complex.

913 **The Hexameric λP-DnaB Complex is Inchoate.**

914 The six copies of λP in the B_6P_6 complex (Figures 9 and 10) are differentially
915 ordered in our EM maps. Domains I and II of each chain are entirely disordered.
916 Only domains III and IV of the four copies (chains Z, Y, W, and V) are visible in our
917 maps. The arrangement of these two domains in B_6P_5 is nearly identical to that in
918 the five copies of λP in B_6P_5. For chains U and X, only the lasso domain IV is
919 visible. The ajar planar DnaB configuration in B_6P_6 explains the pattern of ordered
920 and disordered domain IIIs. The chain U λP domain III is disordered in our maps,
921 and efforts to position it by superposition reveal a steric clash with corresponding
922 domains from chain V and chain Z; similarly for chain X, which would clash with

923 chains W and Y (Figure 10 and Supplementary Figure 22). These clashes arise
924 from the planar nature of DnaB in B_6P_6, which restricts the space available to
925 accommodate the domains III seen in B_6P_5. We also speculate that disorder in the
926 λP protomers may indicate that the loader ensemble is inchoate and has not yet
927 formed the stabilizing interfaces seen in the B_6P_5 entity.

928 The disorganized state of the λP protomers in B_6P_6 extends to the interfaces
929 formed with DnaB (Figure 10A). First, the lack of a breach in the DnaB CTD layer
930 obscures binding site #1 for the chain Z N-terminal lasso/domain I. The disordered
931 domain IIs do not permit the population of site #2, and changes to the NTD layer
932 in B_6P_6 also abolish site #5. Only λP interfaces at sites #3 and #4 are formed.
933 Moreover, the inchoate nature of B_6P_6 programs the burial of diverse surface area
934 depending on the λP protomer. The four ordered λP domain IIIs each bury less
935 surface area than in B_6P_5 (B_6P_6: ~1200 $Å^2$ vs. B_6P_5: ~1600 $Å^2$), and the amounts
936 buried vary by chain (Y > Z > V >W). Similarly, for the λP domain IV interfaces,
937 chain Y buries more surface area (~1430 $Å^2$) than the other chains (W=V=Z: ~1040
938 $Å^2$, X: ~620 $Å^2$, U: ~610 $Å^2$), but still less, on average, than in B_6P5 (B_6P_6: ~1000
939 $Å^2$ vs. B_6P_5: ~1400 $Å^2$). Both findings indicate a lack of complete engagement of
940 the various λP chains with DnaB. Second, comparing the six B_2P_1 sub-complexes
941 in B_6P_6 reveals a much less rigid arrangement than in B_6P_5 (Supplementary Figure
942 20). Unlike the corresponding superposition with B_6P_5 (Supplementary Figure 14),
943 the DnaB chain excluded from the calculation shows a considerably larger RMSD
944 (B_6P_6: 5.4 Å vs B_6P_5: 0.7 Å). Moreover, while the characteristic
945 rotations/translations of the sheared DH and LH elements are evident in B_6P_6, the

946 underlying values differ considerably between chains compared to B_6P_5 (Figure
947 9D). In considering the significance of these changes, the current 3.85 Å resolution
948 of B_6P_6 should be kept in mind.

949 Taken together, analysis of the architecture of DnaB and λP, nucleotide,
950 ssDNA binding sites, and helicase and loader interfaces suggests that B_6P_6
951 represents an early, partially open, inchoate intermediate that can be assigned to
952 a position between the closed planar and open spiral forms in the reaction
953 trajectory (Figure 11).

954 **Discussion**

955 The mechanisms accompanying the loading and activation of the bacterial
956 DnaB helicase at a replication origin are not yet fully understood. To gain insights
957 into these mechanisms, we determined cryo-EM structures of the *E. coli* DnaB• λP
958 helicase loader complex in two oligomeric states, B_6P_5 and B_6P_6. The B_6P_5
959 complex extends an earlier effort at a much lower resolution (33) by shedding light
960 on structural elements that undergo conformation switching during helicase ring
961 opening. The configuration of the pentameric λP ensemble in B_6P_5 also hints at a
962 previously unrecognized autoinhibited intermediate for ssDNA loading. In contrast
963 to the open spiral B_6P_5 entity, the B_6P_6 complex is essentially planar, but with the
964 DnaB CTDs further apart; we refer to this arrangement as the 'ajar planar'
965 configuration. The most economical scheme to sequence these states in the
966 helicase loading pathway is to position them in the following order: a) closed planar
967 DnaB, b) ajar planar B_6P_6, and c) open spiral B_6P_5, followed by other steps (Figure
968 11). We discuss these states in this order.

969 Closed planar DnaB exists in two conformational states, with the NTD and
970 CTD tiers in either dilated or constricted configurations (reviewed in (9, 10, 14–17)
971 and in Supplementary Information), with evidence for a hybrid state (NTD: dilated,
972 CTD: constricted (102)). We observed that six copies of the λP helicase loader
973 bind to closed planar DnaB, stabilizing its CTD tier in the constricted configuration
974 (Figure 11). In contrast, the NTD tier remains dilated. In B_6P_6, both tiers are
975 planar. However, the DnaB CTDs are positioned further apart than in the closed
976 planar form, but not enough to create a breach that exposes the central chamber.
977 The NTD tier is closed. The lack of a breach in ajar planar B_6P_6 DnaB explains
978 the disordered λP N-terminal lasso, whose binding site, which only forms in the
979 open spiral, is blocked (Supplementary Movies 1 and 2). Notably, the crystal
980 structure of the *Bacillus* DnaB-family helicase bound to its DnaI helicase loader
981 also features a 6:6 stoichiometry and a partially open planar DnaB species (110);
982 the relationship between the two complexes, if any, remains to be elucidated.

983 Several lines of evidence suggest that the DnaB and λP components in B_6P_6
984 are still developing and have not reached their final form. First, the six λP
985 protomers exhibit varying order levels in our maps. Each has an ordered C-
986 terminal lasso domain, but two chains are missing domain III, and all chains lack
987 the λP ensemble-stabilizing domain II found in B_6P_5 and the N-terminal
988 lasso/domain I. Six C-terminal lassoes are ordered in B_6P_6, indicating that this
989 segment is likely the first to bind stably to DnaB. Second, the nexus between the
990 DnaB DH and LH elements, representing the binding sites for the C-terminal
991 lassos, exhibits the characteristic rotations/translations seen in the well-defined

992 B_6P_5 entity, but these changes vary by subunit. Moreover, this finding suggests
993 that disruption of the DH-LH interface precedes the breach of one interface and
994 the transition to the open spiral observed in B_6P_5. Third, four of the six λPs in B_6P_6
995 feature ordered domain IIIs bound at CTDs from consecutive DnaB subunits.
996 However, the nature, number of contacts, and buried surface area vary by binding
997 site. Concomitantly, individual CTDs display greater configurational flexibility than
998 in B_6P_5. We presume that the two disordered domain IIIs populate diverse
999 conformations since binding to DnaB is precluded by steric clashes with the
1000 ordered domain IIIs. Fourth, the extensive domain II interface in the B_6P_5 λP
1001 ensemble cannot be accommodated in B_6P_6, leading us to conclude that these
1002 interfaces are unformed and the underlying domain IIs adopt flexible
1003 conformations. Lastly, mismatches in spiral configurations between B_6P_6 and the
1004 translocating open spiral (PDB = 4ESV, (18)) suggest undeveloped ssDNA and
1005 nucleotide-hydrolytic sites.

1006 Transition to the B_6P_5 open spiral complex requires considerable
1007 remodeling of the DnaB and λP entities (Supplementary Movies 1 and 2) and
1008 eviction of one of the λP chains. Both the NTD and CTD tiers are reconfigured.
1009 The planar NTD tier is breached and assumes an open spiral configuration. The
1010 ajar planar CTD tier is remodeled into an open spiral. Remodeling both tiers
1011 creates the complete set of five sites on DnaB for contacts with λP. Breach of the
1012 DnaB ring reveals λP binding site #1. Reconfiguring the DnaB CTDs optimizes
1013 sites #2 and #3 for binding, opening space for two additional λP domain IIIs to bind.
1014 The λP C-terminal lassoes engage more fully with open spiral DnaB at site #4.

1015 Remodeling of the NTD and CTD tiers creates site #5. Although there is room in
1016 the pentameric λP ensemble for a sixth domain II to engage, its corresponding
1017 domain III would have no binding site since binding occurs at DnaB subunit
1018 interfaces, and all the interfaces are occupied. As such, the chain Z N-terminal
1019 lasso binds near the DH helix on the DnaB CTD, where the sixth C-terminal lasso
1020 (chain U) might have been expected to sit. Notably, λP chain Z's multivalent
1021 contacts could also block non-productive DnaB reclosure to the closed planar form.
1022 The finding that the λP loader harbors lasso elements at both the amino and
1023 carboxy termini creates conceptual links with homologs of the DciA loader, which
1024 also feature similar architectures at both termini (7, 27); however, a mechanistic
1025 relationship between λP and these DciA loaders remains to be established.
1026 Remodeling the DnaB CTD tier into the open spiral destroys the DH-LH binding
1027 site for the chain U C-terminal lasso. We speculate that the lack of binding sites
1028 for chain U domains III and the C-terminal lasso destabilizes its presence in the
1029 complex, causing it to be evicted as B_6P_6 matures into B_6P_5.

1030 Although DnaB in B_6P_5 exhibits openings in the NTD and CTD tiers of
1031 sufficient size, the combination of contacts by the N-terminal and C-terminal lasso
1032 domains of λP-chain Z and the extensive interface formed by the five λP domain
1033 IIs precludes entry of physiological origin-derived ssDNA into the inner chamber.
1034 Deepening the mystery is the finding that the B_6P_5 complex still binds ssDNA. We
1035 speculate that ssDNA may bind to the λP ensemble (38) or to the exterior of DnaB,
1036 as previously suggested (107, 108), or both, before the necessary conformational
1037 changes that enable loading of ssDNA in DnaB's inner chamber.

1038 Prior studies have shown that B_6P_5 must undergo additional remodeling as
1039 the helicase loading and activation reaction progresses. The complex must
1040 engage with the octameric λO initiator protein – Oriλ DNA complex (40, 41). We
1041 speculate that four disordered λP N-terminal lassoes (chains V, W, X, and Y) may
1042 have a role in engaging with the λO ensemble, where each lasso engages with two
1043 λO subunits in the λO-λP-DnaB complex. We speculate that the autoinhibition will
1044 be relieved as the B_6P_5 complex is recruited to the λO•Oriλ complex at the
1045 replication origin (Figure 9) and may require intervention by the bacterial heat
1046 shock/chaperone proteins: DnaK, DnaJ, and GrpE (45–48). Among other
1047 questions to be addressed are: Does ssDNA populate a secondary binding site on
1048 the surface of DnaB before entering the central chamber? How and when does
1049 ssDNA enter the central chamber of DnaB? How is the λO-λP-DnaB complex
1050 further reconfigured to activate the helicase for unwinding? The critical roles
1051 played by the *E. coli* chaperones DnaK, DnaJ, and GrpE in additional remodeling
1052 and eviction events remain to be clarified.
1053

Data Availability

Coordinates from the X-ray structure of λP – domain III and the cryo-EM structure of the *E. coli* DnaB–λP complex are available from the RCSB Protein Data Bank under accession codes 8V9S (λP – domain III), 8V9T (B_6P_5-2.84 Å), 9OA1 (B_6P_5-2.66 Å), and 9AO2 (B_6P_6-3.85 Å). The underlying primary data, X-ray detector diffraction images, structure factors, and cryo-EM maps are available from the Protein Data Bank, the SBGrid Data Bank, and the EMBD under the accession codes EMD-43086 (B_6P_5-2.84 Å), EMD-70269 (B_6P_5-2.66 Å), and EMD-70271 (B_6P_6-3.85 Å).

Author Contributions

DB, AS, and DJ conceptualized the study. DB and AS designed and prepared all the proteins. DB and EI performed crystallization and X-ray crystallography. AS performed all the ATPase assays. AS and JC acquired and analyzed the cryo-EM data. All nMS analyses were performed by PDBO in the BTC lab. DB, AS, JC, and DJ jointly built and analyzed the structures and drafted the manuscript.

Funding

This work was supported by the National Science Foundation (DJ: MCB 1818255), the National Institutes of Health (DJ: GM08416 and BTC: P41 GM109824 and P41 GM103314), and the Department of Education (JC: PA200A150068). Some of this work was performed at the Simons Electron Microscopy Center and National Resource for Automated Molecular Microscopy located at the New York Structural Biology Center, supported by grants from the Simons Foundation (SF349247), NYSTAR, and the NIH National Institute of General Medical Sciences (GM103310) with additional support from Agouron

Institute (F00316), NIH (OD019994), and NIH (RR029300). This work is based on research conducted at the Northeastern Collaborative Access Team beamlines, which are funded by the National Institute of General Medical Sciences of the National Institutes of Health (P30 GM124165). The Eiger 16M detector on 24-ID-E is funded by an NIH-ORIP HEI grant (S10OD021527). This research utilized resources from the Advanced Photon Source, a U.S. Department of Energy (DOE) Office of Science User Facility operated by Argonne National Laboratory under Contract No. DE-AC02-06CH11357. Funding for the open charge: National Science Foundation MCB #1818255.

Acknowledgments

We thank the Jeruzalmi lab members, the biophysics group at City College, the CUNY Advanced Science Research Center, and the New York Structural Biology Center for scientific and technical advice. We dedicate our work on the DnaB–λP complex to the memory of Professor Roger McMacken, on whose shoulders we stand and who inspired us in so many ways.

Conflicts of Interest

The authors have no financial or non-financial conflicts of interest.

1098 ## Figures/Figure legends

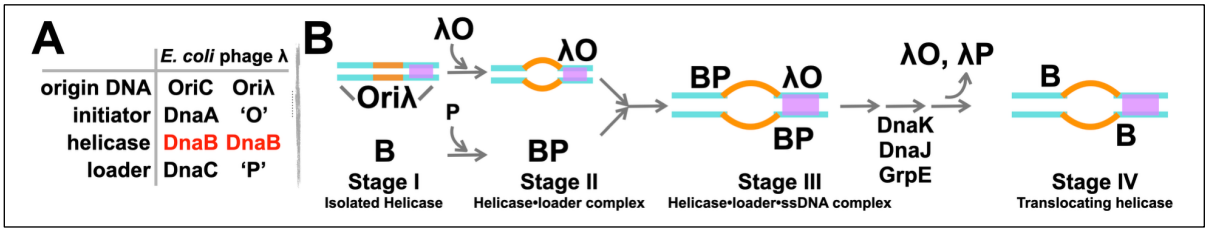

1099 **Figure 1. Loading of the bacterial replicative helicase during the initiation of**
1100 **DNA replication.** A) Molecules associated with initiating DNA replication in *E. coli*
1101 and phage λ. Both systems utilize *E. coli* DnaB (red). B) The loading of the
1102 bacterial DnaB helicase onto the origin DNA occurs at the nexus of two pathways:
1103 their products merge into the complete initiation complex at the replication origin
1104 (17, 111, 112). The first sub-complex is the oligomeric initiator protein complex (*E.*
1105 *coli:* DnaA or phage λ: O) formed at the corresponding replication origin (the four
1106 λO sites are colored in purple); a key outcome of this complex is the initial melting
1107 of the origin's DNA unwinding element (DUE, orange). Capture and remodeling of
1108 the DnaB helicase (designated with the letter 'B') by the helicase loader (*E. coli:*
1109 DnaC or phage λ: P) produces the second sub-complex (BP). These two pathways
1110 converge with the delivery of the loader-bound helicase to the origin. The resulting
1111 initiator-helicase-loader complex at the origin is stabilized by interactions between
1112 the initiator, helicase, and loader (1, 8, 113, 114). A series of additional binding
1113 and remodeling events, including the engagement of the bacterial chaperones
1114 DnaK, DnaJ, and GrpE, culminate in assembling a pair of replication forks (not
1115 shown).

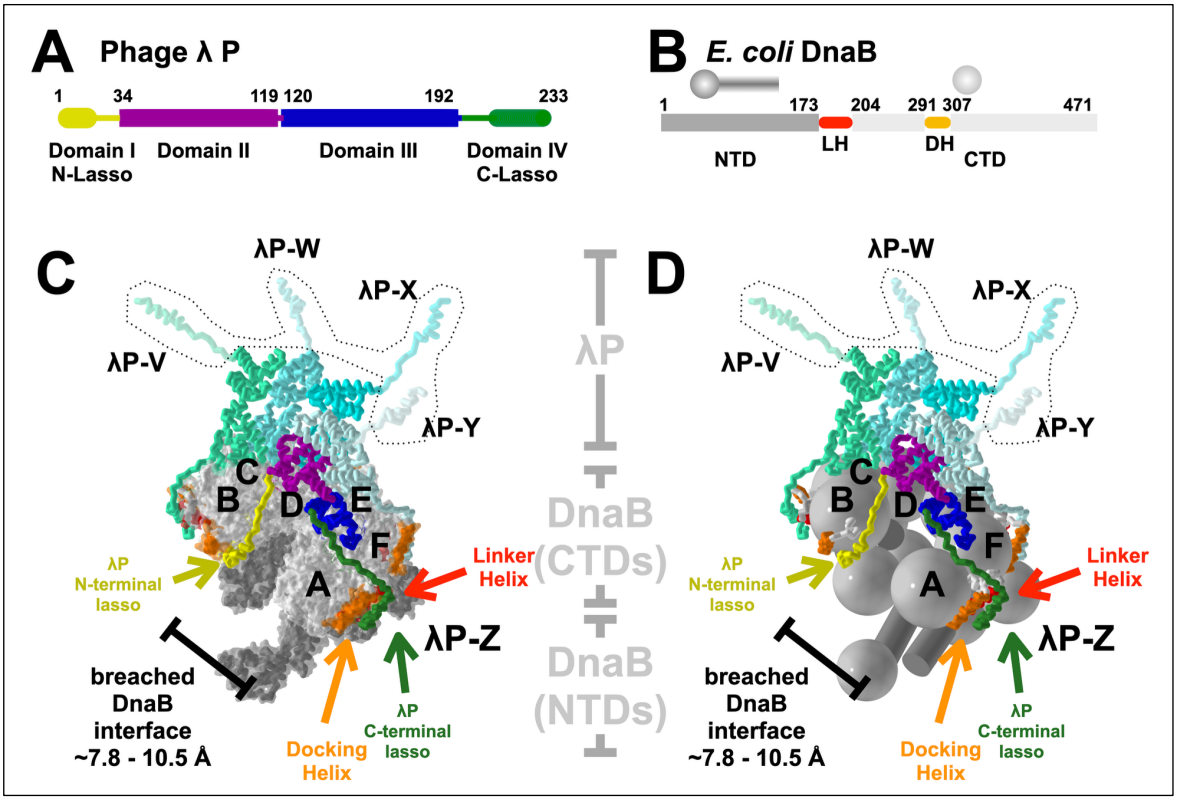

Figure 2. The Structure of the B_6P_5 Form of the *E. coli* DnaB – λP Loader. Linear domain architecture of λP (A) and *E. coli* DnaB (B). The amino (NTD) and carboxy-terminal (CTD) layers of DnaB are depicted using a design language that presents the CTDs as large spheres and the NTDs as small spheres/cylinders. C) The DnaB–λP complex, with its five loader molecules (labeled V, W, X, Y, and Z), is depicted in the ribbon representation and colored in shades of blue, save for chain Z, which is colored by domain as illustrated in panel A. The right-handed open spiral of DnaB is depicted as a surface. The DnaB NTD tier is colored in dark gray, and the CTD layer is in light gray, with the DH and LH elements colored and labeled in orange and yellow. The positions of λP domain I for chains V, W, X, and Y (outlined with a dashed line shape), which are not visible in our maps, are modeled for reference. D) Same as panel C, except that DnaB is depicted using

the above design language. The CTD spheres of each subunit carry labels corresponding to the underlying chain.

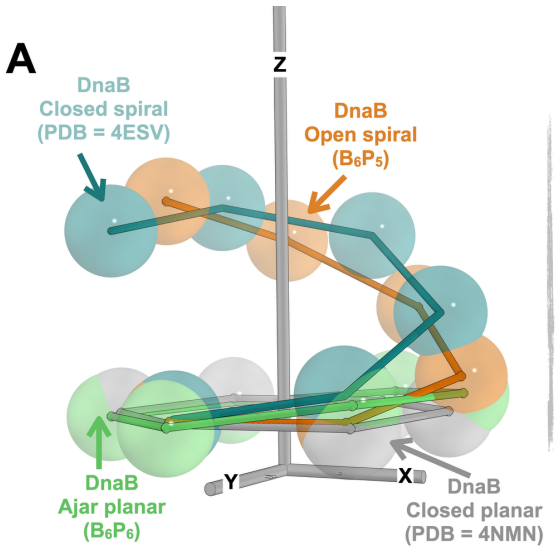

B

DnaB State	Pitch (Å)	Rise (Å)	Twist (°)
Closed Planar (PDB: 4NMN)	0	0	61
Ajar Planar (B_6P_6)	2.0	0.5	60
Open Spiral (B_6P_5)	12.6	3.7	56.4
Closed Spiral (PDB: 4ESV)	19.1	5.4	60.1

Figure 3. States Populated by the DNA-Binding CTD Tier of DnaB. A) The spirals of the CTD layer of the closed planar form (PDB: 4NMN (12), grey), the ajar planar (B_6P_6, this work, green), the open spiral (B_6P_5, this work, orange), and the closed spiral (PDB:4ESV (18), deep teal) are displayed. Individual CTDs, depicted as spheres centered around the gravity of the CTD, are interconnected. The underlying coordinates of each DnaB structure were superimposed onto the CTD of the closed planar structure at the bottom of the spiral. The plane of the CTD tier of the closed planar structure is oriented perpendicular to the Z-axis. B) Helical parameters (pitch, rise, and twist) for the specified states of the DnaB CTD.

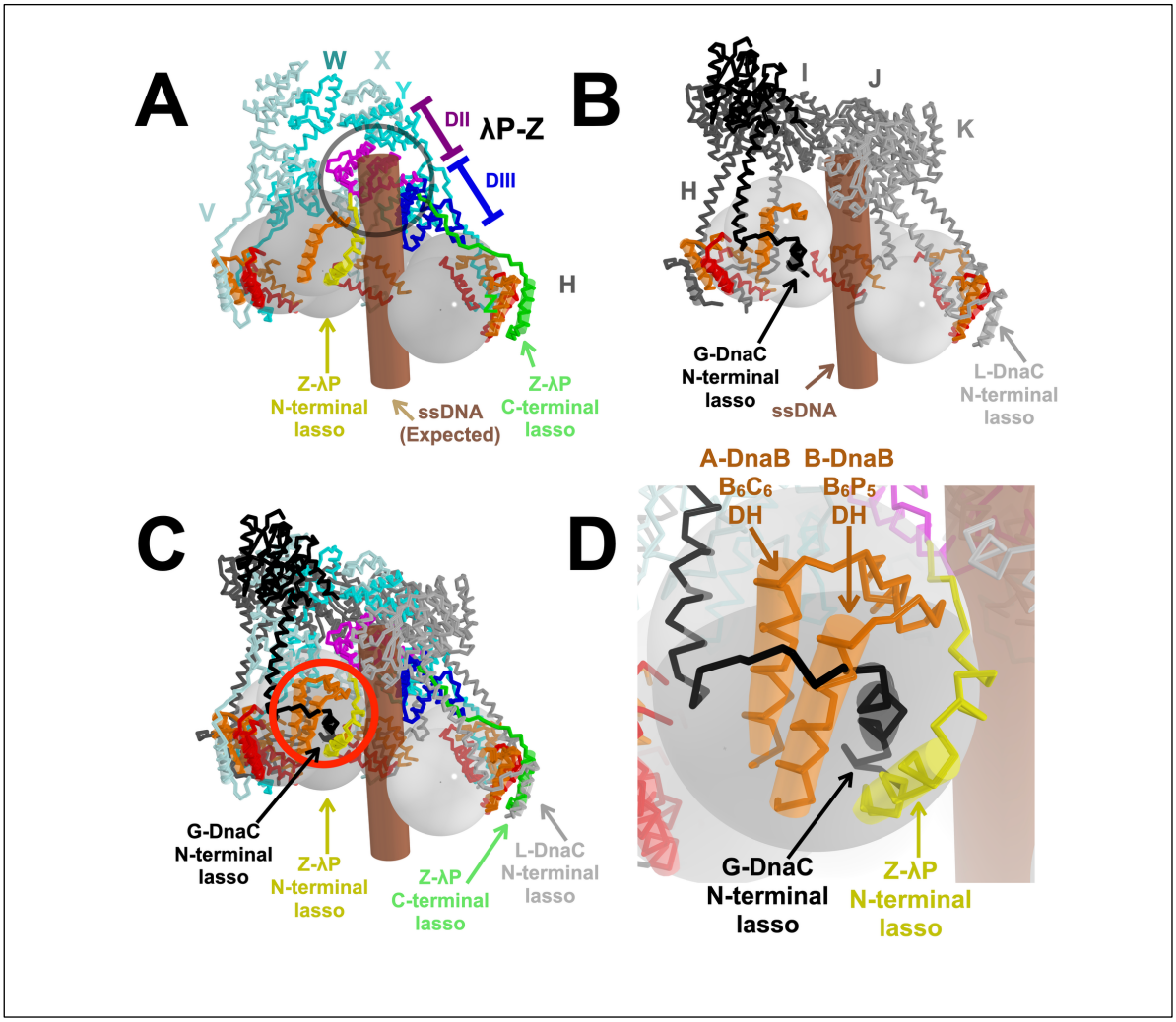

Figure 4. Asymmetry and Convergent Evolution in the λP ensemble. A) In contrast to the other chains, which bind to two DnaB subunits, λP chain Z binds to three subunits (chains B, A, and F), two (chains A and B) located on either side of the breached DnaB interface. λP chain Z is colored by domain (domain I, yellow; domain II, light purple; domain III, blue; domain IV, green), and the remaining λP chains are colored in shades of cyan. The brown cylinder represents the expected position of ssDNA based on the DnaB-DnaC-ssDNA complex (PDB: 6QEM, (34)). The DnaB CTDs are depicted as grey spheres with labels corresponding to the underlying chain; the NTD domains are not shown for clarity. The DnaB DH and

LH helices are colored in red and orange. This disposition of the amino-terminal domain (domains I/II) of λP chain Z effectively precludes entry of a physiological origin ssDNA into the central chamber of DnaB (highlighted by the molecular clash, which is circled in gray). B) The DnaB-DnaC-ssDNA complex (PDB: 6QEM) is posed as superimposed on chain A of the BP complex and depicted in the same style as the B_6P_5 complex in panel A. Individual DnaC protomers are colored in shades of gray. C) The B_6P_5 and B_6C_6 loader complexes in panels A and B are superimposed. Each of the C-terminal lassos from λP superimposes on a DnaC lasso. However, the single visible λP N-terminal lasso overlaps with the position of the DnaC lasso (chain G) at the top of the spiral (circled in red). Thus, one λP subunit (chain Z) forms contacts made by two DnaC loader subunits (chains G and L). D) Close-up of the red-circled segment in panel C.

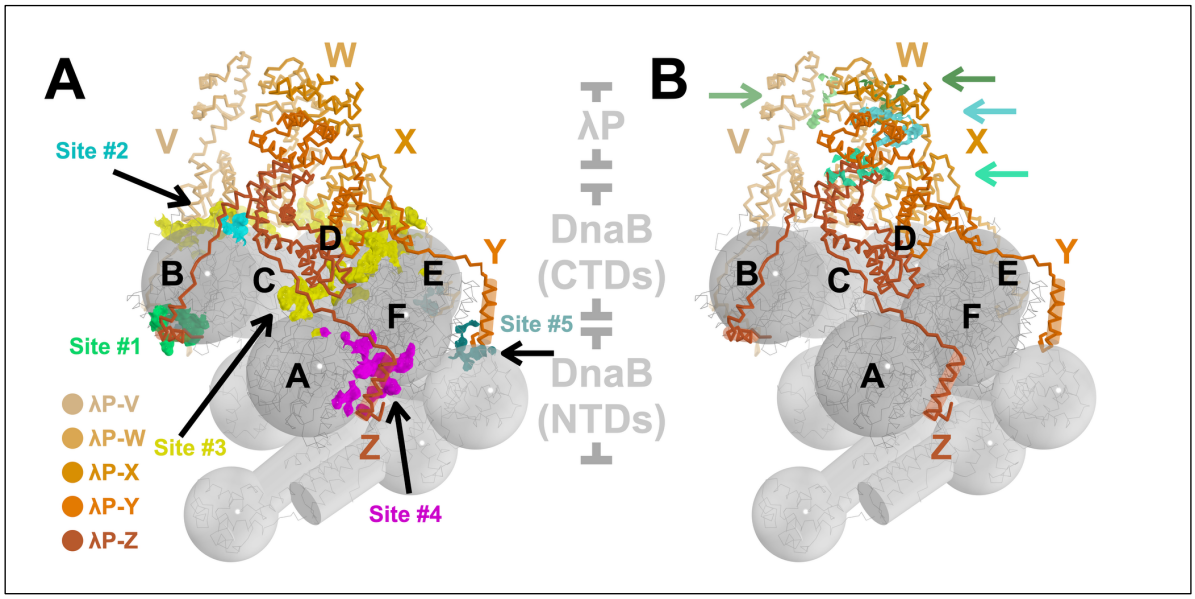

1162 **Figure 5. Five Widely Dispersed Sites Comprise the Interface between λP**
1163 **and *E. coli* DnaB. A)** The five interaction sites (#1-#5, each uniquely colored)
1164 between the loader and helicase subunits. These interaction sites are depicted as
1165 surfaces, with points on the surface indicating positions within 4.5 Å between the
1166 helicase and the loader. Due to the asymmetry of the B_6P_5 complex, not every
1167 loader protomer utilizes each site. The λP ensemble is shown in ribbon format,
1168 colored in shades of orange as indicated in the legend. The DnaB hexamer,
1169 labeled from A to F, is presented in ribbon, sphere, and cylinder design language.
1170 Labels distinguish the CTD spheres. B) The B_6P_5 complex is depicted as in panel
1171 A, except that the interfaces between λP loader subunits are highlighted and
1172 indicated with arrows in the same color as the surface. Interaction sites between
1173 loader subunits are represented as surfaces, with points on the surface indicating
1174 positions within 4.5 Å between pairs of loader subunits.

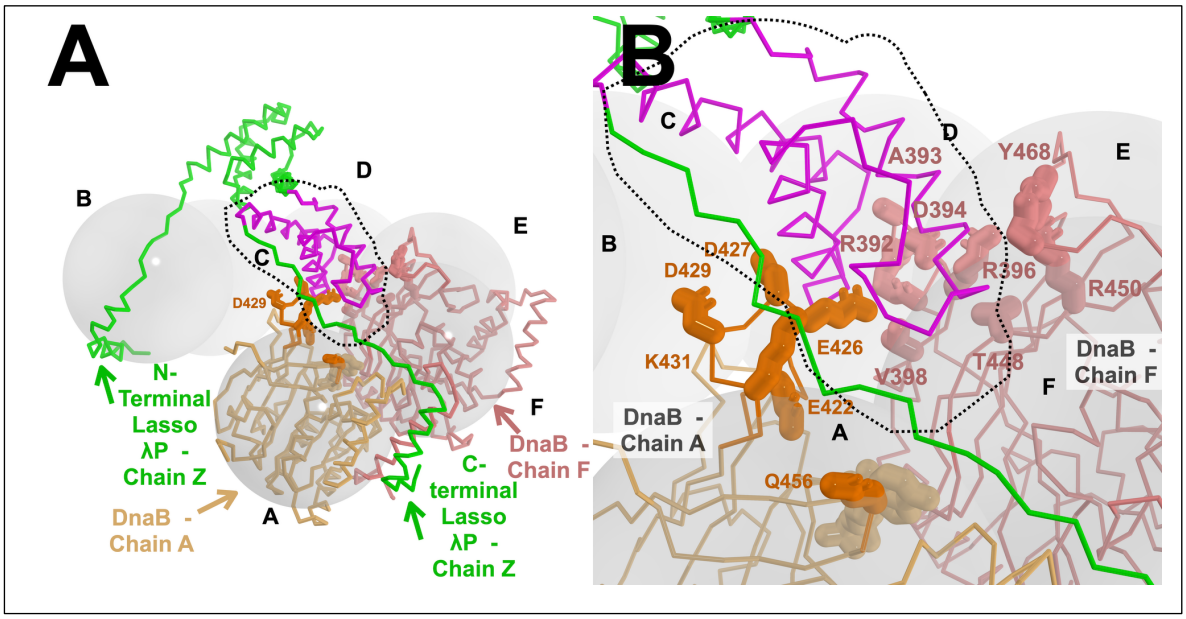

1175 **Figure 6. Stabilization of the DnaB Spiral by Domain III of λP in the B_6P_5**
1176 **complex.** A) The open spiral of DnaB in the B_6P_5 complex is stabilized through
1177 interactions with domain III of the λP loader. The CTDs of DnaB within the B_6P_5
1178 complex are represented by transparent, labeled gray spheres. Chain Z of the λP
1179 ensemble (green) is depicted in the PyMol ribbon representation, along with the
1180 CTDs from chain A (light orange) and chain F (salmon). Residues in the DnaB
1181 CTD from chain A (light orange) and chain F (salmon) that interact with domain III
1182 of λP (outlined) are shown using the stick representation. The corresponding
1183 interfacial residues on chain λP Z are not displayed for clarity. The interface from
1184 the DnaB-DnaC complex (PDB: 6QEL, (34) and Supplementary Figure 15) does
1185 not exhibit such features. B) Close-up view of the area outlined in panel A.
1186

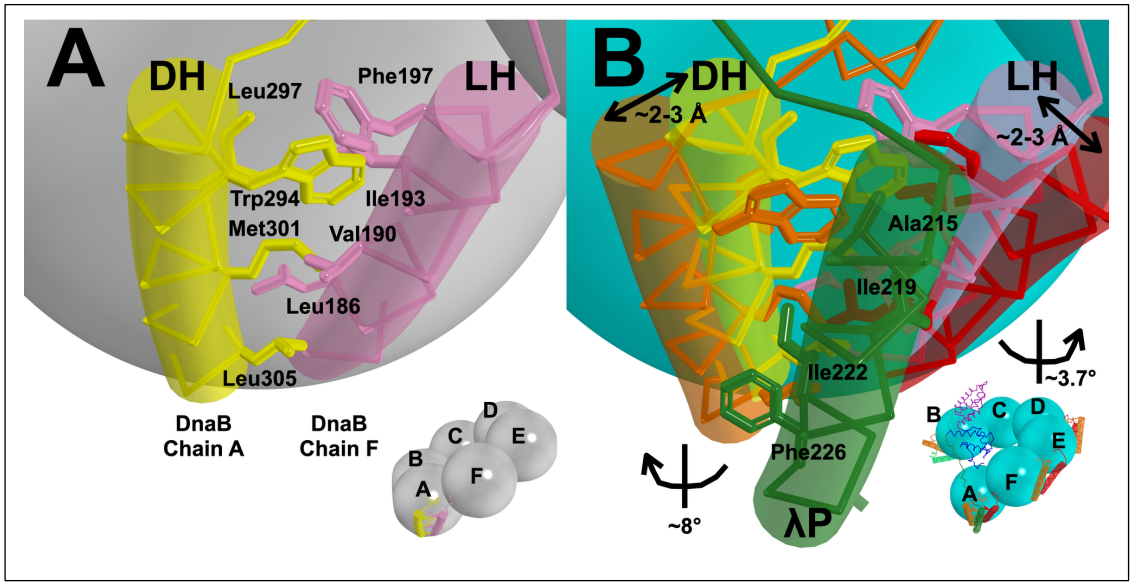

1187 **Figure 7. The Carboxy-Terminal Lassoes of the λP Ensemble in the B_6P_5**
1188 **Complex Shear the DH-LH Elements.** A) Knobs and holes packing between the
1189 docking helix (DH) and linker helix (LH) in the closed planar form of DnaB. The
1190 above model was constructed by superimposing DH and LH helices from the
1191 Alphafold model of *E. coli* DnaB (72) on the closed planar DnaB model (PDB:
1192 4NMN, (12)). Residues 291:306 (DH) and 182:199 (LH) are depicted in the PyMol
1193 ribbon and transparent cylindrical cartoon representation. Interacting residues are
1194 shown as sticks and labeled. B) The C-terminal lasso of the λP loader disrupts the
1195 DH–LH interaction during the transition from the closed planar to the open spiral
1196 form of DnaB in the B_6P_5 complex. The DH and LH helices rotate an average of
1197 8° and 3.7° away from the dimer interface as they move apart by 2-3 Å during the
1198 transition. The closed planar DH–LH interaction is disrupted and replaced by new
1199 interactions (residues shown as sticks and labeled) with the C-terminal lasso helix
1200 of λP. These interactions are found at each λP C-terminal lasso. Panel insets
1201 depict the relevant DnaB hexamer with each CTD drawn as a sphere; for clarity,

1202 the NTD domains are not shown. The letters on each inset represent protein chains

1203 of the DnaB hexamer.

1204

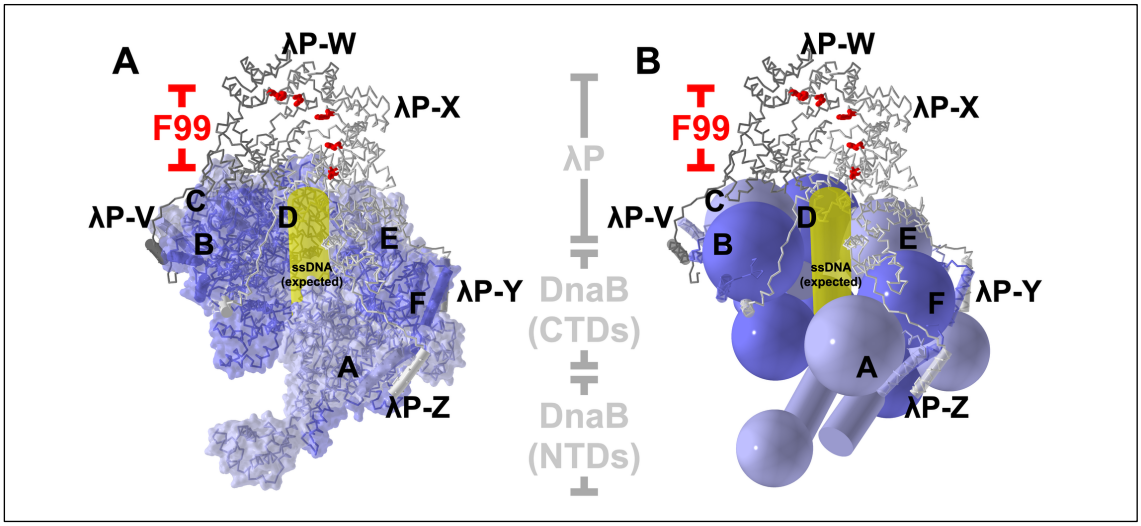

Figure 8. Path of ssDNA through the B_6P_5 complex. λP Phe 99 (red) is known to crosslink with ssDNA (38, 106). Within the B_6P_5 complex, the five instances of λP Phe 99 circumscribe a volume enclosed by the five copies of λP domain II. The constellation of λP Phe 99 residues is above the volume anticipated to be occupied by ssDNA (yellow), based on the DnaB•DnaC-ssDNA complex (PDB: 6QEM (34)). A) The B_6P_5 complex is illustrated in a ribbon representation. DnaB is shown with a transparent surface colored in alternating blue hues. B) The same orientation of the B_6P_5 complex, but with DnaB depicted using the sphere and cylinder design language.

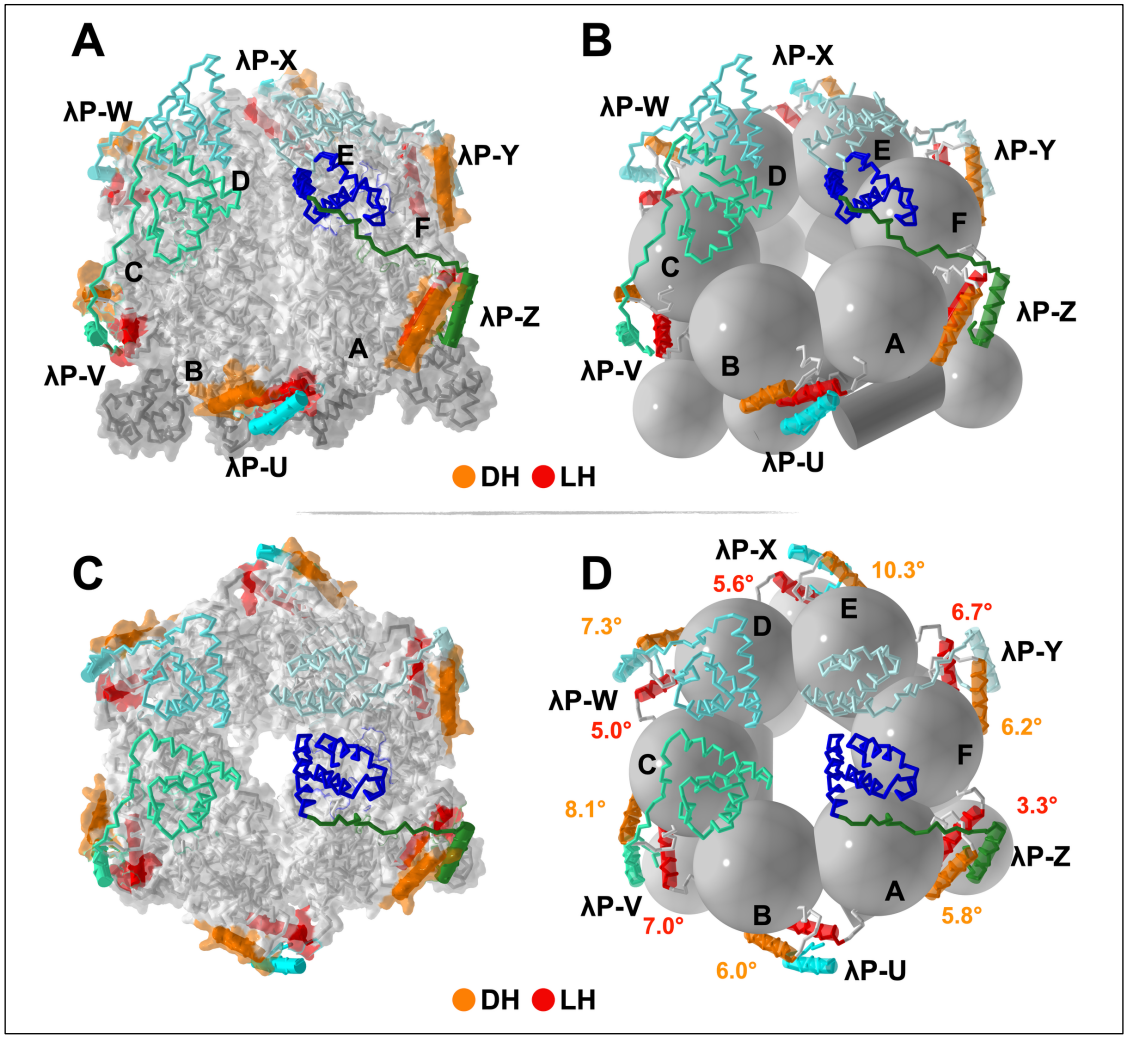

1215 **Figure 9. The Structure of the B_6P_6 Form of the *E. coli* DnaB–λP loader.** In all
1216 the panels, the B_6P_6 complex, with its six loader molecules (labeled U, V, W, X, Y,
1217 and Z), is depicted in the ribbon representation; domains III and IV of λP chain Z
1218 are colored in blue and green; the other chains in hues of blue. DnaB in panels A
1219 and C is shown as a surface. Panels B and D illustrate DnaB using the sphere
1220 and cylinder design language. The DH and LH elements in each panel are shown
1221 in the ribbon and cylinder format and are colored orange and yellow. Panels A
1222 and B are rotated by 45° along the horizontal X-axis compared to the pose in
1223 panels C and D. The orange and red values in panel D represent rotation angles

experienced by the DH and LH elements in the transition from closed planar to ajar planar.

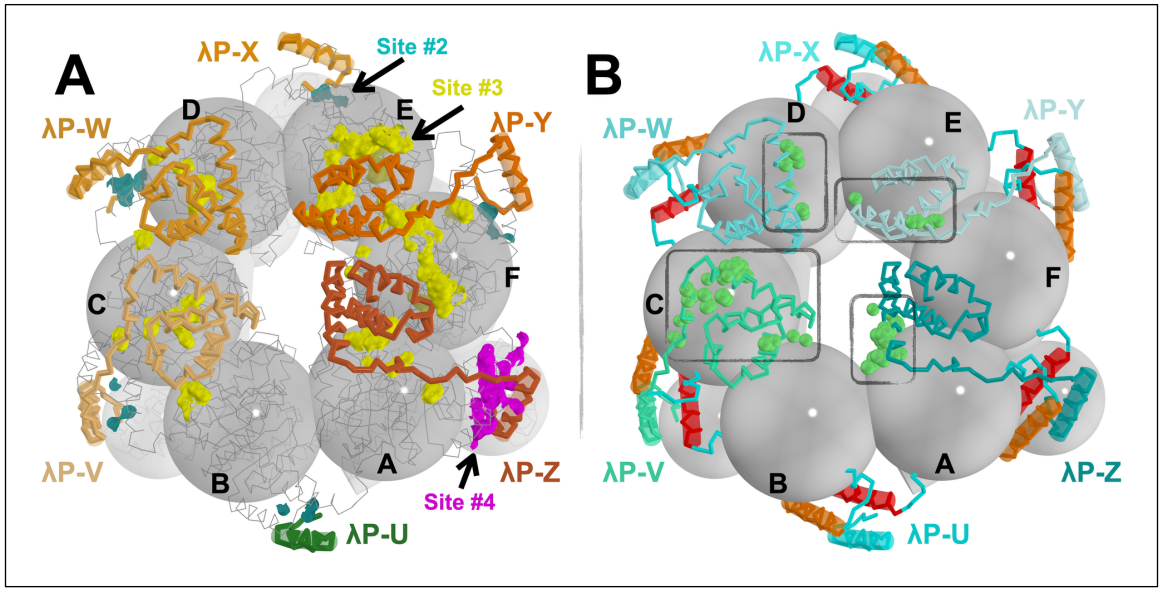

1227 **Figure 10. The Helicase Loader Interface in the B_6P_6 Complex is Inchoate. A)**
1228 The interaction sites (#2, #3, and #4, each uniquely colored) between DnaB and
1229 λP. As in Figure 5, the interaction sites are depicted as surfaces, with points on
1230 the surface indicating positions within 4.5 Å between the helicase and the loader.
1231 Sites #3 (yellow) and #4 (purple) encompass different amounts of buried surface
1232 area in the various interfaces. The λP ensemble is shown in ribbon format, colored
1233 in shades of orange. The DnaB hexamer, labeled from A to F, is presented in a
1234 ribbon and the sphere/cylinder design language. The CTD spheres of each
1235 subunit carry labels corresponding to the underlying chain. B) Incompatibility of
1236 the disordered domain IIIs of chain U and X with the B_6P_6 complex is indicated by
1237 the clash (close approach; within 1.5 Å) with chains W and Y, and V and Z. The
1238 light-green-colored spheres show atomic positions in the above chains within 1.5
1239 Å of chains U and X. The complete superposition appears in Supplementary
1240 Figure 23.
1241

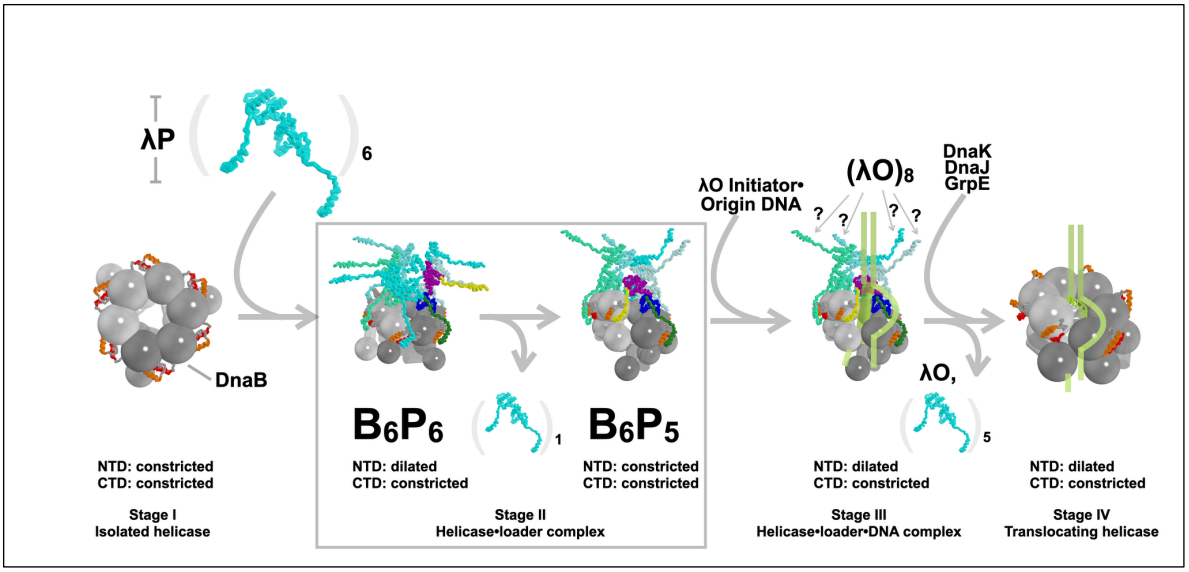

Figure 11. Model for loading the DnaB-λP loader complex onto the λO-Oriλ. Assembly stages of the DnaB helicase at the phage λ origin. This work focused on the two oligomeric forms of the BP complex (boxed) that populate Stage II: B_6P_6 and B_6P_5. Six copies of the λP loader bind to the closed planar ring (Stage I) of *E. coli* DnaB, creating the ajar-planar B_6P_6 complex. In this complex, the λP domains I (chain Z), II, and III have not adopted the configuration in B_6P_5. Loss of one copy of the λP loader accompanies reconfiguration into the B_6P_5 open spiral. This entity features openings in the NTD and CTD layers that allow ssDNA to enter the central chamber. However, the λP chain-Z binds on both sides of the breached interface in DnaB, stabilized by a substantial interface between the domain IIs of the λP pentamer. This configuration effectively blocks the entry of replication-origin-derived ssDNA into DnaB's inner chamber. Despite the blockage, the B_6P_5 complex can still bind ssDNA; it is suggested that this binding may occur outside of DnaB's inner chamber in Stage III. The disordered domain Is of λP chains V, W, X, and Y are proposed to bind to the λO-Oriλ initiator-replication origin complex.

1257 The expulsion of the λP ensemble, assisted by *E. coli* chaperone proteins,
1258 facilitates the transition to Stage IV, the translocating form. The yellow cylinder
1259 represents the expected path of ssDNA inferred from the DnaB•DnaC-ssDNA
1260 complex (PDB: 6QEM, (34)). The docking helix and linker helix elements are
1261 colored red and orange.
1262

1263 ## References
1264
1265

1266 1. Bleichert,F., Botchan,M.R. and Berger,J.M. (2017) Mechanisms for initiating
1267 cellular DNA replication. *Science*, **355**, eaah6317.

1268 2. Katayama,T. (2017) DNA Replication, From Old Principles to New
1269 Discoveries. *Adv. Exp. Med. Biol.*, **1042**, 79–98.

1270 3. Yao,N.Y. and O'Donnell,M.E. (2016) Evolution of replication machines. *Critical*
1271 *Reviews in Biochemistry and Molecular Biology*, **51**, 135–149.

1272 4. Yao,N. and O'Donnell,M. (2016) Bacterial and Eukaryotic Replisome
1273 Machines. *JSM biochemistry and molecular biology*, **3**.

1274 5. Greci,M.D. and Bell,S.D. (2020) Archaeal DNA Replication. *Annu Rev*
1275 *Microbiol*, **74**, 1–16.

1276 6. Trakselis,M.A. (2016) Structural Mechanisms of Hexameric Helicase Loading,
1277 Assembly, and Unwinding. *F1000Research*, **5**.

1278 7. Blaine,H.C., Simmons,L.A. and Stallings,C.L. (2023) Diverse Mechanisms of
1279 Helicase Loading during DNA Replication Initiation in Bacteria. *J. Bacteriol.*,
1280 **205**, e00487-22.

1281 8. Katayama,T. and Nagata,T. (1991) Initiation of chromosomal DNA replication
1282 which is stimulated without oversupply of DnaA protein in Escherichia coli.
1283 *Molecular & general genetics : MGG*, **226**, 491–502.

1284 9. O'Donnell,M.E. and Li,H. (2018) The ring-shaped hexameric helicases that
1285 function at DNA replication forks. *Nat. Struct. Mol. Biol.*, **25**, 122–130.

1286 10. Fernandez,A.J. and Berger,J.M. (2021) Mechanisms of hexameric helicases.
1287 *Crit Rev Biochem Mol*, 10.1080/10409238.2021.1954597.

1288 11. Wang,G., Klein,M.G., Tokonzaba,E., Zhang,Y., Holden,L.G. and Chen,X.S.
1289 (2008) The structure of a DnaB-family replicative helicase and its interactions
1290 with primase. *Nat Struct Mol Biol*, **15**, 94–100.

1291 12. Strycharska,M.S., Arias-Palomo,E., Lyubimov,A.Y., Erzberger,J.P.,
1292 O'Shea,V.L., Bustamante,C.J. and Berger,J.M. (2013) Nucleotide and Partner-
1293 Protein Control of Bacterial Replicative Helicase Structure and Function. *Mol.*
1294 *Cell*, **52**, 844–854.

1295 13. Bailey,S., Eliason,W.K. and Steitz,T.A. (2007) Structure of hexameric DnaB
1296 helicase and its complex with a domain of DnaG primase. *Science (New York,*
1297 *NY)*, **318**, 459–463.

1298 14. Zhang,Z., Chen,J., Yao,M. and Wang,G. (2025) Structural Insight Into the
1299 Function of DnaB Helicase in Bacterial DNA Replication. *Proteins: Struct.,*
1300 *Funct., Bioinform.*, **93**, 420–429.

1301 15. Chase,J., Berger,J. and Jeruzalmi,D. (2022) Convergent evolution in two
1302 bacterial replicative helicase loaders. *Trends Biochem Sci*, **47**, 620–630.

1303 16. Oakley,A.J. (2019) A structural view of bacterial DNA replication. *Protein Sci*,
1304 **28**, 990–1004.

1305 17. Kaguni,J.M. (2018) The Macromolecular Machines that Duplicate the
1306 Escherichia coli Chromosome as Targets for Drug Discovery. *Antibiotics*, **7**,
1307 23.

1308 18. Itsathitphaisarn,O., Wing,R.A., Eliason,W.K., Wang,J. and Steitz,T.A. (2012)
1309 The Hexameric Helicase DnaB Adopts a Nonplanar Conformation during
1310 Translocation. *Cell*, **151**, 267–277.

1311 19. Kaguni,J.M. (2014) Molecular Life Sciences, An Encyclopedic Reference. In
1312 Molecular Life Sciences. Springer New York, pp. 1–14.

1313 20. Velten,M., McGovern,S., Marsin,S., Ehrlich,S.D., Noirot,P. and Polard,P.
1314 (2003) A Two-Protein Strategy for the Functional Loading of a Cellular
1315 Replicative DNA Helicase. *Mol Cell*, **11**, 1009–1020.

1316 21. Brézellec,P., Vallet-Gely,I., Possoz,C., Quevillon-Cheruel,S. and Ferat,J.-L.
1317 (2016) DciA is an ancestral replicative helicase operator essential for bacterial
1318 replication initiation. *Nature communications*, **7**, 13271.

1319 22. Brézellec,P., Petit,M.-A., Pasek,S., Vallet-Gely,I., Possoz,C. and Ferat,J.-L.
1320 (2017) Domestication of lambda phage genes into a putative third type of
1321 Replicative Helicase Matchmaker. *Genome Biol Evol*, **9**, evx111.

1322 23. Marsin,S., Adam,Y., Cargemel,C., Andreani,J., Baconnais,S., Legrand,P.,
1323 Li de la Sierra-Gallay,I., Humbert,A., Aumont-Nicaise,M., Velours,C., *et al.*
1324 (2021) Study of the DnaB:DciA interplay reveals insights into the primary
1325 mode of loading of the bacterial replicative helicase. *Nucleic Acids Res*,
1326 10.1093/nar/gkab463.

1327 24. Ozaki,S., Wang,D., Wakasugi,Y., Itani,N. and Katayama,T. (2022) The
1328 Caulobacter crescentus DciA promotes chromosome replication through

1329 topological loading of the DnaB replicative helicase at replication forks.
1330 *Nucleic Acids Res.*, **50**, gkac1146-.

1331 25. Cargemel,C., Baconnais,S., Aumont-Nicaise,M., Noiray,M., Maurin,L.,
1332 Andreani,J., Walbott,H., Cam,E.L., Ochsenbein,F., Marsin,S., *et al.* (2023)
1333 Structural Insights of the DciA Helicase Loader in Its Relationship with DNA.
1334 *Int J Mol Sci*, **24**, 1427.

1335 26. Cargemel,C., Marsin,S., Noiray,M., Legrand,P., Bounoua,H., Sierra-
1336 Gallay,I.L. de la, Walbott,H. and Quevillon-Cheruel,S. (2023) The LH–DH
1337 module of bacterial replicative helicases is the common binding site for DciA
1338 and other helicase loaders. *Acta Crystallogr. Sect. D*, **79**, 177–187.

1339 27. Blaine,H.C., Burke,J.T., Ravi,J. and Stallings,C.L. (2022) DciA Helicase
1340 Operators Exhibit Diversity across Bacterial Phyla. *J Bacteriol*, **204**, e00163-
1341 22.

1342 28. Jones,C.E., Mueser,T.C., Dudas,K.C., Kreuzer,K.N. and Nossal,N.G. (2001)
1343 Bacteriophage T4 gene 41 helicase and gene 59 helicase-loading protein: A
1344 versatile couple with roles in replication and recombination. *Proc. Natl. Acad.*
1345 *Sci.*, **98**, 8312–8318.

1346 29. Seco,E.M., Zinder,J.C., Manhart,C.M., Piano,A.L., McHenry,C.S. and
1347 Ayora,S. (2013) Bacteriophage SPP1 DNA replication strategies promote viral
1348 and disable host replication in vitro. *Nucleic Acids Res*, **41**, 1711–1721.

1349 30. Odegrip,R., Schoen,S., Haggård-Ljungquist,E., Park,K. and Chattoraj,D.K.
1350 (2000) The Interaction of Bacteriophage P2 B Protein with Escherichia coli
1351 DnaB Helicase. *J. Virol.*, **74**, 4057–4063.

1352 31. O'Shea,V.L. and Berger,J.M. (2014) Loading strategies of ring-shaped
1353 nucleic acid translocases and helicases. *Current Opinion in Structural Biology*,
1354 **25**, 16–24.

1355 32. Davey,M.J. and O'Donnell,M. (2003) Replicative helicase loaders: ring
1356 breakers and ring makers. *Curr Biol*, **13**, R594–R596.

1357 33. Chase,J., Catalano,A., Noble,A.J., Eng,E.T., Olinares,P.D., Molloy,K.,
1358 Pakotiprapha,D., Samuels,M., Chait,B., Georges,A.D., *et al.* (2018)
1359 Mechanisms of opening and closing of the bacterial replicative helicase. *Elife*,
1360 **7**, 1822.

1361 34. Arias-Palomo,E., Puri,N., Murray,V.L.O., Yan,Q. and Berger,J.M. (2019)
1362 Physical Basis for the Loading of a Bacterial Replicative Helicase onto DNA.
1363 *Mol Cell*, **74**, 173-184.e4.

1364 35. Davey,M.J., Fang,L., McInerney,P., Georgescu,R.E. and O'Donnell,M. (2002)
1365 The DnaC helicase loader is a dual ATP/ADP switch protein. *The EMBO*
1366 *journal*, **21**, 3148–3159.

1367 36. Puri,N., Fernandez,A.J., Murray,V.L.O., McMillan,S., Keck,J.L. and
1368 Berger,J.M. (2021) The molecular coupling between substrate recognition and
1369 ATP turnover in a AAA+ hexameric helicase loader. *Elife*, **10**, e64232.

1370 37. Mallory,J.B., Alfano,C. and McMacken,R. (1990) Host virus interactions in the
1371 initiation of bacteriophage lambda DNA replication. Recruitment of Escherichia
1372 coli DnaB helicase by lambda P replication protein. *J. Biol. Chem.*, **265**,
1373 13297–13307.

1374 38. Learn,B.A., Um,S.J., Huang,L. and McMacken,R. (1997) Cryptic single-
1375 stranded-DNA binding activities of the phage lambda P and Escherichia coli
1376 DnaC replication initiation proteins facilitate the transfer of E. coli DnaB
1377 helicase onto DNA. *Proceedings of the National Academy of Sciences of the*
1378 *United States of America*, **94**, 1154–1159.

1379 39. Wegrzyn,K. and Konieczny,I. (2024) Toward an understanding of the DNA
1380 replication initiation in bacteria. *Front. Microbiol.*, **14**, 1328842.

1381 40. Mensa-Wilmot,K., Seaby,R., Alfano,C., Wold,M.C., Gomes,B. and
1382 McMacken,R. (1989) Reconstitution of a nine-protein system that initiates
1383 bacteriophage lambda DNA replication. *The Journal of biological chemistry*,
1384 **264**, 2853–2861.

1385 41. Dodson,M., Echols,H., Wickner,S., Alfano,C., Mensa-Wilmot,K., Gomes,B.,
1386 LeBowitz,J., Roberts,J.D. and McMacken,R. (1986) Specialized nucleoprotein
1387 structures at the origin of replication of bacteriophage lambda: localized
1388 unwinding of duplex DNA by a six-protein reaction. *Proc. Natl. Acad. Sci.*, **83**,
1389 7638–7642.

1390 42. Makowska-Grzyska,M. and Kaguni,J.M. (2010) Primase Directs the Release
1391 of DnaC from DnaB. *Mol Cell*, **37**, 90–101.

1392 43. Polissi,A., Goffin,L. and Georgopoulos,C. (1995) The Escherichia coli heat
1393 shock response and bacteriophage lambda development. *FEMS microbiology*
1394 *reviews*, **17**, 159–169.

1395 44. Zylicz,M. (1993) The Escherichia coli chaperones involved in DNA
1396 replication. *Philos. Trans. R. Soc. Lond. Ser. B: Biol. Sci.*, **339**, 271–278.

1397 45. Zylicz,M., Ang,D., Liberek,K. and Georgopoulos,C. (1989) Initiation of lambda
1398 DNA replication with purified host- and bacteriophage-encoded proteins: the
1399 role of the dnaK, dnaJ and grpE heat shock proteins. *EMBO J.*, **8**, 1601–1608.

46. Liberek,K., Georgopoulos,C. and Zylicz,M. (1988) Role of the Escherichia coli DnaK and DnaJ heat shock proteins in the initiation of bacteriophage lambda DNA replication. *Proc. Natl. Acad. Sci.*, **85**, 6632–6636.

47. Hoffmann,H.J., Lyman,S.K., Lu,C., Petit,M.A. and Echols,H. (1992) Activity of the Hsp70 chaperone complex--DnaK, DnaJ, and GrpE--in initiating phage lambda DNA replication by sequestering and releasing lambda P protein. *Proc. Natl. Acad. Sci.*, **89**, 12108–12111.

48. Osipiuk,J., Georgopoulos,C. and Zylicz,M. (1993) Initiation of lambda DNA replication. The Escherichia coli small heat shock proteins, DnaJ and GrpE, increase DnaK's affinity for the lambda P protein. *J. Biol. Chem.*, **268**, 4821–4827.

49. Orlova,N., Gerding,M., Ivashkiv,O., Olinares,P.D.B., Chait,B.T., Waldor,M.K. and Jeruzalmi,D. (2017) The replication initiator of the cholera pathogen's second chromosome shows structural similarity to plasmid initiators. *Nucleic Acids Res*, **45**, 3724–3737.

50. Bernard,A. and Payton,M. (1995) Fermentation and Growth of Escherichia coli for Optimal Protein Production. *Curr. Protoc. Protein Sci.*, **00**, 5.3.1-5.3.18.

51. Kantardjieff,K.A. and Rupp,B. (2003) Matthews coefficient probabilities: Improved estimates for unit cell contents of proteins, DNA, and protein-nucleic acid complex crystals. *Protein science : a publication of the Protein Society*, **12**, 1865–1871.

52. Otwinowski,Z. and Minor,W. (1997) Processing of X-ray diffraction data collected in oscillation mode. *Macromolecular Crystallography, Pt A*, **276**, 307–326.

53. Liebschner,D., Afonine,P.V., Baker,M.L., Bunkóczi,G., Chen,V.B., Croll,T.I., Hintze,B., Hung,L.W., Jain,S., McCoy,A.J., *et al.* (2019) Macromolecular structure determination using X-rays, neutrons and electrons: recent developments in Phenix. *Acta Crystallographica Section D: Structural Biology*, **75**, 861–877.

54. Emsley,P., Lohkamp,B., Scott,W.G. and Cowtan,K. (2010) Features and development of Coot. *Acta crystallographica Section D, Biological crystallography*, **66**, 486–501.

55. Olinares,P.D.B. and Chait,B.T. (2019) The Eukaryotic RNA Exosome, Methods and Protocols. *Methods Mol. Biol.*, **2062**, 357–382.

56. Reid,D.J., Diesing,J.M., Miller,M.A., Perry,S.M., Wales,J.A., Montfort,W.R. and Marty,M.T. (2019) MetaUniDec: High-Throughput Deconvolution of Native Mass Spectra. *J. Am. Soc. Mass Spectrom.*, **30**, 118–127.

57. Marty,M.T., Baldwin,A.J., Marklund,E.G., Hochberg,G.K.A., Benesch,J.L.P. and Robinson,C.V. (2015) Bayesian Deconvolution of Mass and Ion Mobility Spectra: From Binary Interactions to Polydisperse Ensembles. *Anal. Chem.*, **87**, 4370–4376.

58. Lindsley,J.E. (2000) DNA Topoisomerase Protocols. *Methods Mol Biology Clifton N J*, **95**, 57–64.

59. Kiianitsa,K., Solinger,J.A. and Heyer,W.-D. (2003) NADH-coupled microplate photometric assay for kinetic studies of ATP-hydrolyzing enzymes with low and high specific activities. *Analytical Biochemistry*, **321**, 266–271.

60. Cheng,A., Kim,P.T., Kuang,H., Mendez,J.H., Chua,E.Y.D., Maruthi,K., Wei,H., Sawh,A., Aragon,M.F., Serbynovskyi,V., *et al.* (2023) Fully automated multi-grid cryoEM screening using Smart Leginon. *IUCrJ*, **10**, 77–89.

61. Cheng,A., Negro,C., Bruhn,J.F., Rice,W.J., Dallakyan,S., Eng,E.T., Waterman,D.G., Potter,C.S. and Carragher,B. (2021) Leginon: New features and applications. *Protein Sci.*, **30**, 136–150.

62. Bepler,T., Borst,A.J., Bouvette,J., Cannone,G., Chen,S., Cheng,A., Cheng,A., Fan,Q., Grollios,F., Gupta,H., *et al.* (2022) Smart data collection for CryoEM. *J Struct Biol*, **214**, 107913.

63. Noble,A.J., Dandey,V.P., Wei,H., Brasch,J., Chase,J., Acharya,P., Tan,Y.Z., Zhang,Z., Kim,L.Y., Scapin,G., *et al.* (2018) Routine single particle CryoEM sample and grid characterization by tomography. *eLife*, **7**, e34257.

64. Punjani,A. and Fleet,D.J. (2023) 3DFlex: determining structure and motion of flexible proteins from cryo-EM. *Nat Methods*, **20**, 1–11.

65. Punjani,A. and Fleet,D.J. (2021) 3D variability analysis: Resolving continuous flexibility and discrete heterogeneity from single particle cryo-EM. *J Struct Biol*, **213**, 107702.

66. Punjani,A., Rubinstein,J.L., Fleet,D.J. and Brubaker,M.A. (2017) cryoSPARC: algorithms for rapid unsupervised cryo-EM structure determination. *Nature Methods*, **14**, 290–296.

67. Punjani,A., Zhang,H. and Fleet,D.J. (2020) Non-uniform refinement: adaptive regularization improves single-particle cryo-EM reconstruction. *Nat. Methods*, **17**, 1214–1221.

68. Punjani,A., Rubinstein,J., Fleet,D. and Brubaker,M. (2017) Protocol for rapid unsupervised cryo-EM structure determination using cryoSPARC software. *Protoc Exch*, 10.1038/protex.2017.009.

69. Sanchez-Garcia,R., Gomez-Blanco,J., Cuervo,A., Carazo,J.M., Sorzano,C.O.S. and Vargas,J. (2021) DeepEMhancer: a deep learning solution for cryo-EM volume post-processing. *Commun Biology*, **4**, 874.

70. Bepler,T., Morin,A., Rapp,M., Brasch,J., Shapiro,L., Noble,A.J. and Berger,B. (2019) Positive-unlabeled convolutional neural networks for particle picking in cryo-electron micrographs. *Nat Methods*, **16**, 1153–1160.

71. Fass,D., Bogden,C.E. and Berger,J.M. (1999) Crystal structure of the N-terminal domain of the DnaB hexameric helicase. *Structure (London, England : 1993)*, **7**, 691–698.

72. AlphaFold-Protein-Structure-Database (2022) Alphafold Monomer V2.0 Prediction For Replicative DnaB Helicase; Title: 2 (A0a771b6f2).

73. Jumper,J., Evans,R., Pritzel,A., Green,T., Figurnov,M., Ronneberger,O., Tunyasuvunakool,K., Bates,R., Žídek,A., Potapenko,A., *et al.* (2021) Highly accurate protein structure prediction with AlphaFold. *Nature*, **596**, 583–589.

74. Varadi,M., Anyango,S., Deshpande,M., Nair,S., Natassia,C., Yordanova,G., Yuan,D., Stroe,O., Wood,G., Laydon,A., *et al.* (2021) AlphaFold Protein Structure Database: massively expanding the structural coverage of protein-sequence space with high-accuracy models. *Nucleic Acids Res*, **50**, D439–D444.

75. Adams,P.D., Afonine,P.V., Bunkóczi,G., Chen,V.B., Davis,I.W., Echols,N., Headd,J.J., Hung,L.-W., Kapral,G.J., Grosse-Kunstleve,R.W., *et al.* (2010) PHENIX: a comprehensive Python-based system for macromolecular structure solution. *Acta crystallographica Section D, Biological crystallography*, **66**, 213–221.

76. Afonine,P.V., Poon,B.K., Read,R.J., Sobolev,O.V., Terwilliger,T.C., Urzhumtsev,A. and Adams,P.D. (2018) Real-space refinement in PHENIX for cryo-EM and crystallography. *Acta Crystallogr Sect D*, **74**, 531–544.

77. Vagin,A. and Teplyakov,A. (2010) Molecular replacement with MOLREP. *Acta crystallographica Section D, Biological crystallography*, **66**, 22–25.

78. Agirre,J., Atanasova,M., Bagdonas,H., Ballard,C.B., Baslé,A., Beilsten-Edmands,J., Borges,R.J., Brown,D.G., Burgos-Mármol,J.J., Berrisford,J.M., *et al.* (2023) The CCP4 suite: integrative software for macromolecular crystallography. *Acta Crystallogr. Sect. D*, **79**, 449–461.

79. Emsley,P. and Cowtan,K. (2004) Coot: model-building tools for molecular graphics. *Acta crystallographica Section D, Biological crystallography*, **60**, 2126–2132.

80. Winn,M.D., Ballard,C.C., Cowtan,K.D., Dodson,E.J., Emsley,P., Evans,P.R., Keegan,R.M., Krissinel,E.B., Leslie,A.G.W., McCoy,A., *et al.* (2011) Overview of the CCP4 suite and current developments. *Acta crystallographica Section D, Biological crystallography*, **67**, 235–242.

81. Brown,A., Long,F., Nicholls,R.A., Toots,J., Emsley,P. and Murshudov,G. (2015) Tools for macromolecular model building and refinement into electron cryo-microscopy reconstructions. *Acta crystallographica Section D, Biological crystallography*, **71**, 136–153.

82. Kleywegt,G., Zou,J., Kjeldgaard,M. and Jones,T. (2001) International Tables for Crystallography, Vol. F, edited by MG Rossmann & E. Arnold, ch. 17.1, pp. 353ą356, 366ą367.

83. Sierk,M. and Kleywegt,G. (2004) Deja Vu All Over Again: Finding and Analyzing Protein Structure Similarities. *Structure (London, England : 1993)*, **12**, 2103–2111.

84. Kleywegt,G.J. (2007) Quality control and validation. *Methods in molecular biology (Clifton, NJ)*, **364**, 255–272.

85. Kleywegt,G. and Jones,T. (1997) Model building and refinement practice. *Macromolecular Crystallography, Pt A*, **277**, 208–230.

86. Pettersen,E.F., Goddard,T.D., Huang,C.C., Couch,G.S., Greenblatt,D.M., Meng,E.C. and Ferrin,T.E. (2004) UCSF Chimera--a visualization system for exploratory research and analysis. *Journal of computational chemistry*, **25**, 1605–1612.

87. Williams,C.J., Headd,J.J., Moriarty,N.W., Prisant,M.G., Videau,L.L., Deis,L.N., Verma,V., Keedy,D.A., Hintze,B.J., Chen,V.B., *et al.* (2018) MolProbity: More and better reference data for improved all-atom structure validation. *Protein Sci.*, **27**, 293–315.

88. Echols,N., Moriarty,N.W., Klei,H.E., Afonine,P.V., Bunkóczi,G., Headd,J.J., Mccoy,A.J., Oeffner,R.D., Read,R.J., Terwilliger,T.C., *et al.* (2014) Automating crystallographic structure solution and refinement of protein-ligand complexes. *Acta crystallographica Section D, Biological crystallography*, **70**, 144–154.

89. Zwart,P.H., Afonine,P.V., Grosse-Kunstleve,R.W., Hung,L.-W., Ioerger,T.R., Mccoy,A.J., McKee,E., Moriarty,N.W., Read,R.J., Sacchettini,J.C., *et al.*

(2008) Automated structure solution with the PHENIX suite. *Methods in molecular biology (Clifton, NJ)*, **426**, 419–435.

90. Terwilliger,T.C., Read,R.J., Adams,P.D., Brunger,A.T., Afonine,P.V. and Hung,L.-W. (2013) Model morphing and sequence assignment after molecular replacement. *Acta Crystallogr. Sect. D: Biol. Crystallogr.*, **69**, 2244–2250.

91. Afonine,P.V., Grosse-Kunstleve,R.W., Echols,N., Headd,J.J., Moriarty,N.W., Mustyakimov,M., Terwilliger,T.C., Urzhumtsev,A., Zwart,P.H. and Adams,P.D. (2012) Towards automated crystallographic structure refinement with phenix.refine. *Acta crystallographica Section D, Biological crystallography*, **68**, 352–367.

92. Schrodinger-LLC (2024) The PyMOL Molecular Graphics System, Version 3.0.

93. Morin,A., Eisenbraun,B., Key,J., Sanschagrin,P.C., Timony,M.A., Ottaviano,M. and Sliz,P. (2013) Collaboration gets the most out of software. *eLife*, **2**, e01456.

94. Cruz,M.J. de la and Eng,E.T. (2023) Scaling up cryo-EM for biology and chemistry: The journey from niche technology to mainstream method. *Structure*, 10.1016/j.str.2023.09.009.

95. Saibil,H.R. (2022) Cryo-EM in molecular and cellular biology. *Mol Cell*, **82**, 274–284.

96. Guaita,M., Watters,S.C. and Loerch,S. (2022) Recent advances and current trends in cryo-electron microscopy. *Curr. Opin. Struct. Biol.*, **77**, 102484.

97. Chari,A. and Stark,H. (2023) Prospects and Limitations of High-Resolution Single-Particle Cryo-Electron Microscopy. *Annu. Rev. Biophys.*, **52**, 391–411.

98. Hayes,S., Erker,C., Horbay,M., Marciniuk,K., Wang,W. and Hayes,C. (2013) Phage Lambda P Protein: Trans-Activation, Inhibition Phenotypes and their Suppression. *Viruses*, **5**, 619–653.

99. Chang,S.F., Ng,D., Baird,L. and Georgopoulos,C. (1991) Analysis of an Escherichia coli dnaB temperature-sensitive insertion mutation and its cold-sensitive extragenic suppressor. *J. Biol. Chem.*, **266**, 3654–3660.

100. Leipe,D.D., Aravind,L., Grishin,N.V. and Koonin,E.V. (2000) The bacterial replicative helicase DnaB evolved from a RecA duplication. *Genome Res*, **10**, 5–16.

1573 101. Oakley,A.J. and Xu,Z.Q. (2022) E. coli DnaB bound to ssDNA and
1574 AMPPNP. 10.2210/pdb7t20/pdb.

1575 102. Oakley,A.J. and Xu,Z.Q. (2023) E. coli DnaB bound to ssDNA and ADP-
1576 AlF4. 10.2210/pdb7t21/pdb.

1577 103. Oakley,A.J. and Xu,Z.Q. (2023) E. coli DnaB bound to three DnaG C-
1578 terminal domains, ssDNA, ADP and AlF4. 10.2210/pdb7t22/pdb.

1579 104. Oakley,A.J. and Xu,Z.Q. (2023) E. coli DnaB bound to two DnaG C-terminal
1580 domains, ssDNA, ADP and AlF4. 10.2210/pdb7t23/pdb.

1581 105. Marsin,S., Adam,Y., Cargemel,C., Andreani,J., Baconnais,S., Legrand,P.,
1582 Li de la Sierra-Gallay,I., Humbert,A., Aumont-Nicaise,M., Velours,C., *et al.*
1583 (2021) Study of the DnaB:DciA interplay reveals insights into the primary
1584 mode of loading of the bacterial replicative helicase. *Nucleic Acids Res.*, **49**,
1585 gkab463-.

1586 106. Shao,H. (2006) Mechanism of Loading of DnaB Helicase Molecules at the
1587 Bacteriophage Lambda Replication Origin During Initiation of DNA Replication.
1588 *Ph.D Dissertation (UMI # 3262504), Johns Hopkins University*.

1589 107. Carney,S.M., Gomathinayagam,S., Leuba,S.H. and Trakselis,M.A. (2017)
1590 Bacterial DnaB helicase interacts with the excluded strand to regulate
1591 unwinding. *J Biol Chem*, **292**, 19001–19012.

1592 108. Behrmann,M.S., Perera,H.M., Hoang,J.M., Venkat,T.A., Visser,B.J.,
1593 Bates,D. and Trakselis,M.A. (2021) Targeted chromosomal Escherichia
1594 coli:dnaB exterior surface residues regulate DNA helicase behavior to
1595 maintain genomic stability and organismal fitness. *Plos Genet*, **17**, e1009886.

1596 109. Biswas,T. and Tsodikov,O.V. (2008) Hexameric ring structure of the N-
1597 terminal domain of Mycobacterium tuberculosis DnaB helicase. *The FEBS*
1598 *journal*, **275**, 3064–3071.

1599 110. Liu,B., Eliason,W.K. and Steitz,T.A. (2013) Structure of a helicase-helicase
1600 loader complex reveals insights into the mechanism of bacterial primosome
1601 assembly. *Nature communications*, **4**, 2495.

1602 111. Chodavarapu,S. and Kaguni,J.M. (2016) Replication Initiation in Bacteria.
1603 **39**, 1–30.

1604 112. O'Donnell,M., Langston,L. and Stillman,B. (2013) Principles and concepts of
1605 DNA replication in bacteria, archaea, and eukarya. *Cold Spring Harbor*
1606 *perspectives in biology*, **5**, a010108–a010108.

113. Bell,S.P. and Kaguni,J.M. (2013) Helicase loading at chromosomal origins of replication. *Cold Spring Harbor perspectives in biology*, **5**, a010124.

114. Kaguni,J.M. (2013) DNA Replication: Initiation in Bacteria. In Encyclopedia of Biological Chemistry. Elsevier, pp. 121–125.